International Journal of Solids and Structures 49 (2012) 3838–3852

Contents lists available at SciVerse ScienceDirect

International Journal of Solids and Structures

journal homepage: www.elsevier.com/locate/ijsolstr

Effect of single-crystal plastic deformation mechanisms on the dilatational plastic response of porous polycrystals

Ricardo A. Lebensohn [a,*], Oana Cazacu [b]

[a] Los Alamos National Laboratory, MST8, MS G755, Los Alamos, NM 87545, USA
[b] Department of Mechanical and Aerospace Engineering, University of Florida/REEF Shalimar, FL 32579-1163, USA

ARTICLE INFO

Article history:
Received 1 May 2012
Received in revised form 7 August 2012
Available online 30 August 2012

Keywords:
Porous media
Homogenization
Micromechanics
Dilatational plasticity
Tension–compression asymmetry
Polycrystals

ABSTRACT

In this paper, the combined effects of texture and asymmetric single-crystal plastic deformation mechanisms on the dilatational response of voided polycrystals are assessed for the first time. To this end, a full-field dilatational viscoplastic Fast Fourier Transform (FFT)-based approach is used to generate gauge surfaces for porous polycrystals deforming by twinning at single crystal level, which are compared to yield surfaces obtained according to a recent analytical criterion for porous materials. Both approaches are cross-validated, revealing unusual features of the dilatational response, namely, a lack of symmetry of the surfaces with respect to both the hydrostatic and deviatoric axes. This strong sensitivity to the third invariant of the stress deviator is associated to the anisotropy and the tension–compression asymmetry of the plastic response of the matrix.

1. Introduction

Ductile failure in metals occurs due to the nucleation, growth and coalescence of voids (McClintock, 1968). Voids are nucleated in metals mainly by decohesion at particle–matrix interfaces, or by micro-cracking of second-phase particles (see, for example, Tvergaard, 1981). In materials deforming by mechanical twinning, damage nucleation can also occur at twin boundary intersections with other twin boundaries or grain boundaries (Mahajan, 1981; Livescu et al., 2012). Voids can also nucleate in single crystals that do not contain pre-existing voids or inclusions (see, for example, Cuitino and Ortiz (1996), Lubarda et al. (2004), and the study on cylindrical void growth in rigid-ideally plastic single crystals of Kysar and Gan, 2007). In turn, these nuclei grow and eventually coalesce inside a plastically-deforming matrix. Thus, the ability to accurately describe the evolution of voids in a ductile metal is a key element to accurately predict its failure. Micromechanics-based models pioneered by Rice and Tracey (1969) and Gurson (1977), and later extended by a number of authors (see, for example, Tvergaard, 1981; Tvergaard and Needleman, 1984; Leblond et al., 1994; Garajeu and Suquet, 1997; Gologanu et al., 1997) are successful in describing void growth in an isotropic homogeneous matrix. However, most metallic materials display strong anisotropy and complex heterogeneous microstructure. With few exceptions (e.g. Benzerga and Besson, 2001; Monchiet et al., 2008; Stewart and Cazacu, 2011) coupling between anisotropy and porosity evolution remains largely unexplored. In what concerns microstructural effects on void growth, some of which were recently characterized experimentally (e.g. Escobedo et al., 2011), even fewer theoretical and numerical studies (e.g. Lebensohn et al., 2011) attempted to establish correlations between porosity evolution and the polycrystalline character of the matrix.

In addition to texture-induced anisotropy, for certain polycrystals, a significant tension–compression asymmetry ("strength-differential") is observed although no volume change accompanies yielding. This asymmetry in yielding and strain-hardening behavior is due, e.g. to activation of mechanical twinning (Tomé et al., 2001; Proust et al., 2007; Nixon et al., 2010a,b), or non-Schmid-type slip at the single crystal level (see, for example, Vitek et al., 2004; Groger et al., 2008). In order to approximate the plastic response in the presence of randomly-distributed spherical voids inside such polycrystals, Cazacu and Stewart (2009) carried out a limit analysis of a hollow sphere obeying the isotropic form of Cazacu et al.'s (2006) yield criterion, which is pressure-insensitive, and yet, able to capture "strength-differential" effects. In contrast to Gurson's yield surface, Cazacu and Stewart's (2009) does not display the usual symmetry with respect to the deviatoric axis (i.e. the predicted yield strength under hydrostatic tension is different from the yield strength under hydrostatic compression) and shows sensitivity of the dilatational plastic response to the stress third invariant.

Materials with hexagonal crystal structure (e.g., Ti, Zr, Mg), which are strongly textured display both anisotropy and

* Corresponding author. Tel.: +1 505 665 3035; fax: +1 505 667 8021.
E-mail addresses: lebenso@lanl.gov (R.A. Lebensohn), cazacu@reef.ufl.edu (O. Cazacu).

0020-7683/$ - see front matter © 2012 Elsevier Ltd. All rights reserved.
http://dx.doi.org/10.1016/j.ijsolstr.2012.08.019

tension–compression asymmetry in deformation and strength (Tomé et al., 2001; Proust et al., 2007; Nixon et al., 2010a). Although a lot of progress has been made in the past decade in the characterization and modeling of the basic deformation mechanisms operating in such materials at single crystal level, and how the latter affect the polycrystal behavior (e.g. Proust et al., 2007; Tirry et al., 2011), experimental characterization of ductile damage in such materials is very limited (Gray et al., 2000; Marya et al., 2006; Millett et al., 2008). The existing evidence suggests that the size of the pores is of the same order or larger than the average grain size. Therefore, a representative volume element (RVE) of such materials should consist of a polycrystalline matrix with intergranular voids, and, if the dilatational plasticity problem is to be treated with analytical homogenization, the yield criterion for the matrix should account for the asymmetric plastic response of the fully-dense polycrystal.

To capture the combined effects of anisotropy and tension–compression asymmetry of the matrix on the response of a porous material containing randomly-distributed spherical voids, Stewart and Cazacu (2011) extended Cazacu and Stewart's (2009) formulation, performing analytical homogenization of a hollow sphere obeying the anisotropic Cazacu et al.'s (2006) criterion. In contrast to existing anisotropic yield surfaces for porous materials (e.g. Benzerga and Besson, 2001; Monchiet et al., 2008), the resulting yield surface depends on all the invariants of the stress deviator $\boldsymbol{\sigma}'$, as well as on the mixed invariants of $\boldsymbol{\sigma}'$, and the symmetry tensors associated with orthotropy. Thus, the criterion accounts for the influence of both the direction and the sense of loading on the dilatational plastic response of the material. Finite-element (FE) unit cell calculations were also conducted to verify the upper-bound character Stewart and Cazacu's (2011) criterion and assess its validity. On the other hand, controlled experimental data on the dilatational response of anisotropic materials with "strength-differential" effects, e.g. polycrystals in which twinning is a predominant deformation mechanism, are lacking, so the unusual trends associated to the combined effects of the anisotropy and tension–compression asymmetry remain to be confirmed.

Independently of the aforementioned studies within the framework of limit analysis, Lebensohn et al. (2011) extended a full-field formulation based on Fast Fourier Transforms (FFT) (Moulinec and Suquet, 1998; Michel et al., 2000; Lebensohn, 2001) to study the influence of different microstructural features (overall porosity, texture of the matrix material, single-crystal anisotropy, etc.) and type of loading on the dilatational viscoplastic behavior of voided polycrystals with pre-existing intergranular voids. Numerical predictions obtained with this approach were compared with results for porous non-linear materials obtained with homogenization techniques alternative to Gurson-type approaches, based on the variational formulations of Ponte Castañeda (Ponte Castañeda, 1991, 2002) extended to polycrystals (deBotton and Ponte Castañeda, 1995; Liu and Ponte Castañeda, 2004). While Lebensohn et al. (2011) studied both fcc and hcp polycrystals, they assumed plastic deformation of the constituent grains by slip only, obeying the standard Schmid law, i.e. without considering any source of "strength-differential" at grain level, thus resulting in a macroscopic response also symmetric in tension and compression.

In this paper, the combined effects of texture and specific single-crystal plastic deformation mechanisms responsible for tension–compression asymmetry (namely, twinning) on the dilatational response of voided polycrystals are assessed for the first time. To this end, the FFT-based approach of Lebensohn et al. (2011) is used to generate gauge surfaces for porous polycrystals deforming by twinning at single crystal level while Stewart and Cazacu's (2011) criterion is also applied to describe yielding of analogous porous materials. Both approaches reveal unusual features of the dilatational response, namely, a lack of symmetry of the yield surfaces with respect to both the hydrostatic and deviatoric axes.

2. Analytic anisotropic yield criterion for voided materials with tension–compression asymmetry

Stewart and Cazacu (2011) used the kinematic non-linear homogenization approach of Hill (1967) and Mandel (1972) to derive an analytic criterion for porous materials with anisotropic and incompressible matrix displaying tension–compression asymmetry. This anisotropic yield criterion is of the form:

$$\varphi = \hat{m}^2 \sum_{i=1}^{3} \left(\frac{|\hat{\sigma}_i| - k\hat{\sigma}_i}{\sigma_x^T} \right)^2 + 2f \cosh\left(\frac{3\sigma_m}{h\sigma_x^T} \right) - (1+f^2) = 0, \tag{1}$$

where k is a parameter describing the tension–compression asymmetry of the matrix; h is a parameter that depends on the matrix anisotropy and the sign of the mean stress, σ_m; f is the void volume fraction (porosity); and $\hat{\sigma}_1$, $\hat{\sigma}_2$, $\hat{\sigma}_3$ are the principal values of the transformed stress tensor:

$$\hat{\boldsymbol{\sigma}} = \mathbf{L} : \boldsymbol{\sigma}'. \tag{2}$$

In Eq. (2), $\boldsymbol{\sigma}'$ is the deviator of the Cauchy stress tensor $\boldsymbol{\sigma}$ (i.e. $\boldsymbol{\sigma}' = \boldsymbol{\sigma} - \sigma_m \mathbf{I}$, $\sigma_m = \frac{1}{3}\boldsymbol{\sigma} : \mathbf{I}$, with $\mathbf{I}$ being the second-rank identity tensor), $\mathbf{L}$ is a fourth-rank symmetric tensor describing the anisotropy of the matrix, and ":" denotes the doubled contracted product between two tensors. Let ($\boldsymbol{x}$,$\boldsymbol{y}$,$\boldsymbol{z}$) be the reference frame associated with orthotropy, e.g. in the case of a rolled plate, $\boldsymbol{x}$, $\boldsymbol{y}$ and $\boldsymbol{z}$ represent the unit vectors along the rolling, transverse and normal directions, respectively. Relative to the orthotropy axes, tensor $\mathbf{L}$, represented in contracted Voigt notation, is written as:

$$\boldsymbol{L} = \begin{bmatrix} L_{11} & L_{12} & L_{13} & & & \\ L_{12} & L_{22} & L_{23} & & & \\ L_{13} & L_{23} & L_{33} & & & \\ & & & L_{44} & & \\ & & & & L_{55} & \\ & & & & & L_{66} \end{bmatrix}. \tag{3}$$

In expression (1), σ_x^T is the uniaxial tensile yield stress along a given axis of orthotropy (e.g. the x-direction) of the matrix (fully-dense material) while the constant $\hat{m}$ depends on the anisotropy coefficients L_{ij} and the "strength-differential" parameter k, such that:

$$\hat{m} = \frac{1}{\sqrt{(|\Phi_1| - k\Phi_1)^2 + (|\Phi_2| - k\Phi_2)^2 + (|\Phi_3| - k\Phi_3)^2}}, \tag{4}$$

where:

$$\Phi_1 = \frac{2L_{11} - L_{12} - L_{13}}{3}, \quad \Phi_2 = \frac{2L_{12} - L_{22} - L_{23}}{3}, \quad \Phi_3 = \frac{2L_{13} - L_{23} - L_{33}}{3}. \tag{5}$$

The hydrostatic parameter h is given by:

$$h = \sqrt{\frac{r}{5}(4t_1 + 6t_2)}, \tag{6}$$

with:

$$r = \begin{cases} \frac{1}{\hat{m}^2}\left(\frac{3}{3k^2-2k+3}\right) & \text{if } \sigma_m < 0, \\ \frac{1}{\hat{m}^2}\left(\frac{3}{3k^2+2k+3}\right) & \text{if } \sigma_m \geqslant 0. \end{cases} \tag{7}$$

The scalars t_1 and t_2 involved in the expression of parameter h account for the anisotropy of the matrix and are defined as:

$$t_1 = 3\left(B_{13}B_{23} + B_{12}B_{23} + B_{12}B_{13} + 2B_{12}^2 + 2B_{13}^2 + 2B_{23}^2\right), \tag{8a}$$

$$t_2 = B_{44}^2 + B_{55}^2 + B_{66}^2, \tag{8b}$$

where $\mathbf{B} = (\mathbf{L} : \mathbf{K})^{-1}$, with $\mathbf{K}$ denoting the fourth-rank deviatoric unit tensor, i.e. (in Voigt notation):

$$\mathbf{K} = \begin{bmatrix} 2/3 & -1/3 & -1/3 & & & \\ -1/3 & 2/3 & 1/3 & & & \\ -1/3 & -1/3 & 2/3 & & & \\ & & & 1 & & \\ & & & & 1 & \\ & & & & & 1 \end{bmatrix}. \tag{9}$$

The expressions of the components B_{ij} in terms of the components of the orthotropic tensor $\mathbf{L}$ are given in Appendix A. In the absence of voids ($f = 0$), criterion (1) reduces to the matrix's yield criterion, i.e. the quadratic form of Cazacu et al.'s (2006) orthotropic criterion, denoted hereafter CPB06:

$$\tilde{\sigma}_e = \sigma_x^T, \tag{10}$$

with:

$$\tilde{\sigma}_e = \hat{m}\sqrt{\sum_{i=1}^{3}(|\hat{\sigma}_i| - k\hat{\sigma}_i)^2}. \tag{11}$$

Note that CPB06's effective stress, $\tilde{\sigma}_e$, accounts for the combined effects of tension–compression asymmetry and anisotropy of the matrix, since, for $k \neq 0$ it depends on all the invariants of the stress deviator $\boldsymbol{\sigma}'$, as well as on the mixed invariants of $\boldsymbol{\sigma}'$, and the symmetry tensors associated with orthotropy, namely: $\mathbf{M_1} = \mathbf{x} \otimes \mathbf{x}$, $\mathbf{M_2} = \mathbf{y} \otimes \mathbf{y}$, $\mathbf{M_3} = \mathbf{z} \otimes \mathbf{z}$ (see Cazacu et al., 2006; Boehler, 1987). Consequently, it does not have the symmetry properties of Gurson-type criteria with respect to the deviatoric axis, $\sigma_m = 0$. Indeed, according to criterion (1), for tensile hydrostatic loading, yielding of the porous material occurs when $\sigma_m = \hat{p}_Y^+$, with:

$$\hat{p}_Y^+ = -\frac{\sigma_x^T}{3}\sqrt{\frac{3}{\hat{m}^2(3k^2 + 2k + 3)}\left(\frac{4t_1 + 6t_2}{5}\right)}\ln(f) \tag{12}$$

whereas, for compressive hydrostatic loading, yielding occurs when $\sigma_m = \hat{p}_Y^-$, with:

$$\hat{p}_Y^- = \frac{\sigma_x^T}{3}\sqrt{\frac{3}{\hat{m}^2(3k^2 - 2k + 3)}\left(\frac{4t_1 + 6t_2}{5}\right)}\ln(f) \tag{13}$$

Furthermore, Stewart and Cazacu's (2011) criterion is no longer invariant with respect to the transformation $(\sigma_m, \boldsymbol{\sigma}') \to (\sigma_m, -\boldsymbol{\sigma}')$. To further illustrate this dependence of the yield criterion on the third invariant of the stress deviator $J_3 = \sigma_1'\sigma_2'\sigma_3'$ and on the mixed invariants associated with orthotropy, in what follows we present the expressions corresponding to axisymmetric loading along the x-axis, y-axis and z-axis of orthotropy, respectively. Let σ_1 denote the axial stress and σ_3 denote the lateral stress (i.e. the value of the two principal stresses that are equal). Thus, the von Mises equivalent stress is $\sigma_e = |\sigma_1 - \sigma_3|$, the mean stress is $\sigma_m = (\sigma_1 + 2\sigma_3)/3$, and the third invariant of the stress deviator is $J_3 = \frac{2}{27}(\sigma_1 - \sigma_3)^3$.

(a) Case of axisymmetric loading with axial stress along the x-axis, i.e. $\boldsymbol{\sigma} = \sigma_1(\mathbf{x} \otimes \mathbf{x}) + \sigma_3(\mathbf{y} \otimes \mathbf{y} + \mathbf{z} \otimes \mathbf{z})$:

(a1) For $J_3 \leqslant 0$ (i.e. $\sigma_1 \leqslant \sigma_3$), Eq. (1) reads:

$$\varphi = \begin{cases} \left(\frac{\sigma_x^T}{\sigma_x^C}\right)^2\left(\frac{\sigma_e}{\sigma_x^T}\right)^2 + 2f\cosh\left(\frac{\sigma_m}{\sigma_x^T}\sqrt{\frac{15\hat{m}^2(3k^2-2k+3)}{4t_1+6t_2}}\right) - (1+f^2), & \text{if } \sigma_m < 0, \\ \left(\frac{\sigma_x^T}{\sigma_x^C}\right)^2\left(\frac{\sigma_e}{\sigma_x^T}\right)^2 + 2f\cosh\left(\frac{\sigma_m}{\sigma_x^T}\sqrt{\frac{15\hat{m}^2(3k^2+2k+3)}{4t_1+6t_2}}\right) - (1+f^2), & \text{if } \sigma_m \geq 0 \end{cases} \tag{14a}$$

(a2) For $J_3 \geqslant 0$ (i.e. $\sigma_1 \geqslant \sigma_3$), the yield criterion becomes:

$$\varphi = \begin{cases} \left(\frac{\sigma_e}{\sigma_x^C}\right)^2 + 2f\cosh\left(\frac{\sigma_m}{\sigma_x^T}\sqrt{\frac{15\hat{m}^2(3k^2-2k+3)}{4t_1+6t_2}}\right) - (1+f^2), & \text{if } \sigma_m < 0, \\ \left(\frac{\sigma_e}{\sigma_x^T}\right)^2 + 2f\cosh\left(\frac{\sigma_m}{\sigma_x^T}\sqrt{\frac{15\hat{m}^2(3k^2+2k+3)}{4t_1+6t_2}}\right) - (1+f^2), & \text{if } \sigma_m \geq 0. \end{cases} \tag{14b}$$

with σ_x^T and σ_x^C being the matrix's uniaxial tensile and compressive yield stress along the x-axis, respectively.

(b) Case of axisymmetric loading with axial stress along the y-axis, i.e. $\boldsymbol{\sigma} = \sigma_1(\mathbf{y} \otimes \mathbf{y}) + \sigma_3(\mathbf{x} \otimes \mathbf{x} + \mathbf{z} \otimes \mathbf{z})$:

(b1) For $J_3 \leqslant 0$ (i.e. $\sigma_1 \leqslant \sigma_3$):

$$\varphi = \begin{cases} \left(\frac{\sigma_x^T}{\sigma_y^C}\right)^2\left(\frac{\sigma_e}{\sigma_x^T}\right)^2 + 2f\cosh\left(\frac{\sigma_m}{\sigma_x^T}\sqrt{\frac{15\hat{m}^2(3k^2-2k+3)}{4t_1+6t_2}}\right) - (1+f^2), & \text{if } \sigma_m < 0, \\ \left(\frac{\sigma_x^T}{\sigma_y^C}\right)^2\left(\frac{\sigma_e}{\sigma_x^T}\right)^2 + 2f\cosh\left(\frac{\sigma_m}{\sigma_x^T}\sqrt{\frac{15\hat{m}^2(3k^2+2k+3)}{4t_1+6t_2}}\right) - (1+f^2), & \text{if } \sigma_m \geq 0. \end{cases} \tag{15a}$$

(b2) For $J_3 \geqslant 0$ (i.e. $\sigma_1 \geqslant \sigma_3$):

$$\varphi = \begin{cases} \left(\frac{\sigma_x^T}{\sigma_y^T}\right)^2\left(\frac{\sigma_e}{\sigma_x^T}\right)^2 + 2f\cosh\left(\frac{\sigma_m}{\sigma_x^T}\sqrt{\frac{15\hat{m}^2(3k^2-2k+3)}{4t_1+6t_2}}\right) - (1+f^2), & \text{if } \sigma_m < 0, \\ \left(\frac{\sigma_x^T}{\sigma_y^T}\right)^2\left(\frac{\sigma_e}{\sigma_x^T}\right)^2 + 2f\cosh\left(\frac{\sigma_m}{\sigma_x^T}\sqrt{\frac{15\hat{m}^2(3k^2+2k+3)}{4t_1+6t_2}}\right) - (1+f^2), & \text{if } \sigma_m \geq 0. \end{cases} \tag{15b}$$

where σ_y^T and σ_y^C denote the matrix's uniaxial tensile and compressive yield stresses along the y-axis, respectively.

(c) Case of axisymmetric loading with axial stress along the z-axis, i.e. $\boldsymbol{\sigma} = \sigma_1(\mathbf{z} \otimes \mathbf{z}) + \sigma_3(\mathbf{x} \otimes \mathbf{x} + \mathbf{y} \otimes \mathbf{y})$:

(c1) For $J_3 \leqslant 0$ (i.e. $\sigma_1 \leqslant \sigma_3$):

$$\varphi = \begin{cases} \left(\frac{\sigma_x^T}{\sigma_z^C}\right)^2\left(\frac{\sigma_e}{\sigma_x^T}\right)^2 + 2f\cosh\left(\frac{\sigma_m}{\sigma_x^T}\sqrt{\frac{15\hat{m}^2(3k^2-2k+3)}{4t_1+6t_2}}\right) - (1+f^2), & \text{if } \sigma_m < 0, \\ \left(\frac{\sigma_x^T}{\sigma_z^C}\right)^2\left(\frac{\sigma_e}{\sigma_T}\right)^2 + 2f\cosh\left(\frac{\sigma_m}{\sigma_x^T}\sqrt{\frac{15\hat{m}^2(3k^2+2k+3)}{4t_1+6t_2}}\right) - (1+f^2), & \text{if } \sigma_m \geq 0. \end{cases} \tag{16a}$$

(c2) For $J_3 \geqslant 0$ (i.e. $\sigma_1 \geqslant \sigma_3$):

$$\varphi = \begin{cases} \left(\frac{\sigma_z^T}{\sigma_z^T}\right)^2\left(\frac{\sigma_e}{\sigma_x^T}\right)^2 + 2f\cosh\left(\frac{\sigma_m}{\sigma_x^T}\sqrt{3\hat{m}^2\left(3k^2-2k+3\right)\left(\frac{5}{4t_1+6t_2}\right)}\right) - (1+f^2), & \text{if } \sigma_m < 0, \\ \left(\frac{\sigma_z^T}{\sigma_z^T}\right)^2\left(\frac{\sigma_e}{\sigma_x^T}\right)^2 + 2f\cosh\left(\frac{\sigma_m}{\sigma_x^T}\sqrt{3\hat{m}^2\left(3k^2+2k+3\right)\left(\frac{5}{4t_1+6t_2}\right)}\right) - (1+f^2), & \text{if } \sigma_m \geq 0. \end{cases} \tag{16b}$$

where σ_z^T and σ_z^C are the matrix's uniaxial tensile and compressive yield stresses along the z-axis, respectively. Details of the derivation of expressions (14)-(16) are given in Appendix B.

Note that Stewart and Cazacu's (2011) criterion has different expressions depending on the signs of both J_3 and the mean stress. The combined effects of the matrix's tension–compression asymmetry and its orthotropy are evident by comparing expressions (14)-(16) of the criterion. Note that in the case of axisymmetric loading along the x-axis, the sensitivity to J_3 results from the matrix tension–compression asymmetry along the x-axis (i.e. due to

$\sigma_x^C \neq \sigma_x^T$). For axisymmetric loading along the y-axis, the sensitivity to J_3 is due to the matrix tension–compression asymmetry along the y-direction of orthotropy (i.e. due to $\sigma_y^C \neq \sigma_y^T$), while for axisymmetric loading along the z-axis, the sensitivity to J_3 results from the matrix tension–compression asymmetry along the z-axis (i.e. due to $\sigma_z^C \neq \sigma_z^T$). In other words, the sensitivity to J_3 is due to the tension–compression asymmetry ratio in the direction of the applied axial stress.

If there is no tension–compression asymmetry in the matrix (i.e. $k = 0$), $\hat{p}_Y^+ = |\hat{p}_Y^-|$, and Stewart and Cazacu's (2011) criterion reduces to Benzerga and Besson (2001) (for more details, see Stewart and Cazacu, 2011).

If the matrix is isotropic, the anisotropy tensor $\mathbf{L}$ reduces to the fourth-rank identity tensor $\mathbf{I_4}$, i.e. $L_{ijkl} = \frac{1}{2}(\delta_{ik}\delta_{jl} + \delta_{il}\delta_{jk})$, Eq. (2) gives $\hat{\boldsymbol{\sigma}} = \boldsymbol{\sigma}'$, and the matrix has the same uniaxial strength in any direction i.e. $\sigma_x^T = \sigma_y^T = \sigma_z^T \overset{\text{def}}{\equiv} \sigma_T$ and $\sigma_x^C = \sigma_y^C = \sigma_z^C \overset{\text{def}}{\equiv} \sigma_C$, respectively. Replacing the latter in Eq. (5) gives: $\Phi_1 = 2/3, \Phi_2 = \Phi_3 = -1/3$, and, further replacing these values in Eqs. (4), (7) and (8), respectively, we obtain:

$$\hat{m}|_{\mathbf{L}=\mathbf{I_4}} = \sqrt{\frac{9}{2(3k^2 - 2k + 3)}}, \tag{17}$$

$$\mathrm{r}|_{\mathbf{L}=\mathbf{I_4}} = \begin{cases} 2/3, & \text{if } \sigma_m < 0, \\ \frac{2}{3}\cdot\frac{3k^2-2k+3}{3k^2+2k+3} & \text{if } \sigma_m \geqslant 0. \end{cases} \tag{18}$$

$$\mathbf{B} = \mathbf{K} \Rightarrow t_1 = t_2 = 3. \tag{19}$$

Thus, Stewart and Cazacu's (2011) anisotropic yield criterion (Eq. (1)) reduces to Cazacu and Stewart's (2009) isotropic criterion, i.e.

$$m^2 \sum_{i=1}^{3} \left(\frac{|\sigma_i'| - k\sigma_i'}{\sigma_T} \right)^2 + 2f \cosh\left(z_s \frac{3\sigma_m}{2\sigma_T} \right) - (1 + f^2) = 0, \tag{20}$$

with the material constants m and z_s depending only on "strength-differential" parameter k, i.e.

$$m = \sqrt{\frac{9}{2(3k^2 - 2k + 3)}}, \tag{21}$$

$$z_s = \begin{cases} 1 & \text{if } \sigma_m < 0, \\ \sqrt{\frac{3k^2+2k+3}{3k^2-2k+3}} & \text{if } \sigma_m \geqslant 0. \end{cases} \tag{22}$$

Because Cazacu and Stewart's (2009) yield criterion (Eq. (20)) depends on all principal values of the stress deviator and on the sign of the applied mean stress through the parameter z_s, it does not have the symmetry properties of Gurson's (1977) criterion. Specifically, the yield locus (20) is not symmetric with respect to the deviatoric axis. For tensile hydrostatic loading, yielding of the porous material occurs when $\sigma_m = p_Y^T$ (see Eq. (12)), with:

$$p_Y^T \overset{\text{def}}{\equiv} \hat{p}_Y^+|_{\mathbf{L}=\mathbf{I_4}} = -\frac{2}{3}\sigma_C \ln(f), \tag{23}$$

while for compressive hydrostatic loading, yielding occurs when $\sigma_m = p_Y^C$, (see Eq. (13)), with:

$$p_Y^C \overset{\text{def}}{\equiv} \hat{p}_Y^-|_{L=I_4} = \frac{2}{3}\sigma_T \ln(f). \tag{24}$$

Due to the tension–compression asymmetry of the matrix, Cazacu and Stewart's (2009) criterion has different expressions depending on the signs of both J_3 and the mean stress. The expressions of this criterion for axisymmetric loading are easily obtained by setting $\mathbf{L} = \mathbf{I_4}$ in either one of Eqs. (14–16). Thus, for axisymmetric loading, $\boldsymbol{\sigma} = \sigma_1(\mathbf{x}\otimes\mathbf{x}) + \sigma_3(\mathbf{y}\otimes\mathbf{y} + \mathbf{z}\otimes\mathbf{z})$,Cazacu and Stewart's (2009) reads:

(1) For $J_3 \leqslant 0$ (i.e. $\sigma_1 \leqslant \sigma_3$):

$$\varphi = \begin{cases} \left(\frac{\sigma_T}{\sigma_C}\right)^2 \left(\frac{\sigma_e}{\sigma_T}\right)^2 + 2f\cosh\left(\frac{3}{2}\frac{\sigma_m}{\sigma_T}\right) - (1+f^2), & \text{if } \sigma_m < 0, \\ \left(\frac{\sigma_T}{\sigma_C}\right)^2 \left(\frac{\sigma_e}{\sigma_T}\right)^2 + 2f\cosh\left(\frac{3}{2}\frac{\sigma_m}{\sigma_T}\sqrt{\frac{3k^2+2k+3}{3k^2-2k+3}}\right) - (1+f^2), & \text{if } \sigma_m \geq 0, \end{cases} \tag{25a}$$

(2) For $J_3 \geqslant 0$ (i.e. $\sigma_1 \geqslant \sigma_3$):

$$\varphi = \begin{cases} \left(\frac{\sigma_e}{\sigma_T}\right)^2 + 2f\cosh\left(\frac{3}{2}\frac{\sigma_m}{\sigma_T}\right) - (1+f^2), & \text{if } \sigma_m < 0, \\ \left(\frac{\sigma_e}{\sigma_T}\right)^2 + 2f\cosh\left(\frac{3}{2}\frac{\sigma_m}{\sigma_T}\sqrt{\frac{3k^2+2k+3}{3k^2-2k+3}}\right) - (1+f^2), & \text{if } \sigma_m \geq 0. \end{cases} \tag{25b}$$

Furthermore, if the matrix material presents no tension–compression asymmetry in its plastic response ($\sigma_T = \sigma_C$), then: $k = 0$, $z_s = 1$, $m = \sqrt{3/2}$, and the Cazacu and Stewart's (2009) criterion (Eq. (20)) reduces to Gurson's (1977) criterion, i.e.

$$\left(\frac{\sigma_e}{\sigma_T}\right)^2 + 2f\cosh\left(\frac{3}{2}\frac{\sigma_m}{\sigma_T}\right) - (1+f^2) = 0. \tag{26}$$

Finally, if the porosity f is equal to zero, Cazacu and Stewart's (2009) yield criterion reduces to the isotropic form of the quadratic CPB06 (Cazacu et al., 2006) yield criterion, i.e.

$$m\sqrt{\sum_{i=1}^{3}(|\sigma_i'| - k\sigma_i')^2} = \sigma_T. \tag{27}$$

In Section 4, the anisotropic criterion (1) will be applied to the description of the anisotropy and asymmetry of the yield loci of voided fcc polycrystals deforming only by twinning, and hcp polycrystals deforming by slip and twinning, and compared to the predictions of the full-field dilatational viscoplastic model of Lebensohn et al. (2011), described next.

3. Full-field dilatational viscoplastic approach for voided polycrystal

The FFT-based full-field formulation for viscoplastic polycrystals, conceived for periodic unit cells, was originally developed (Moulinec and Suquet, 1998; Michel et al., 2000) as a fast algorithm to compute the elastic and elastoplastic effective and local response of composites, then adapted (Lebensohn, 2001; Lebensohn et al., 2005, 2008, 2009) to deal with the viscoplastic deformation of power-law fully-dense (incompressible) polycrystals, and later extended to the case of dilatational viscoplasticity of porous polycrystals (Lebensohn, 2001), which is reminded in what follows.

3.1. Unit cell construction

We start by describing the construction of the unit cells utilized in this study. The fully-dense polycrystals considered here are periodic, consisting of single crystal grains generated by Voronoi tessellation, whose orientations were randomly chosen from different sets (see below), to reproduce the required overall crystallographic textures. In the case of voided polycrystals, intergranular cavities were also randomly seeded until reaching the required porosity. First, to generate the fully-dense polycrystals, 1000 grain nuclei were randomly distributed in a cubic domain and, to ensure periodicity, they were periodically replicated immediately outside the cube. In turn, the cubic domain was partitioned into a regular grid of Fourier points (in all the examples that

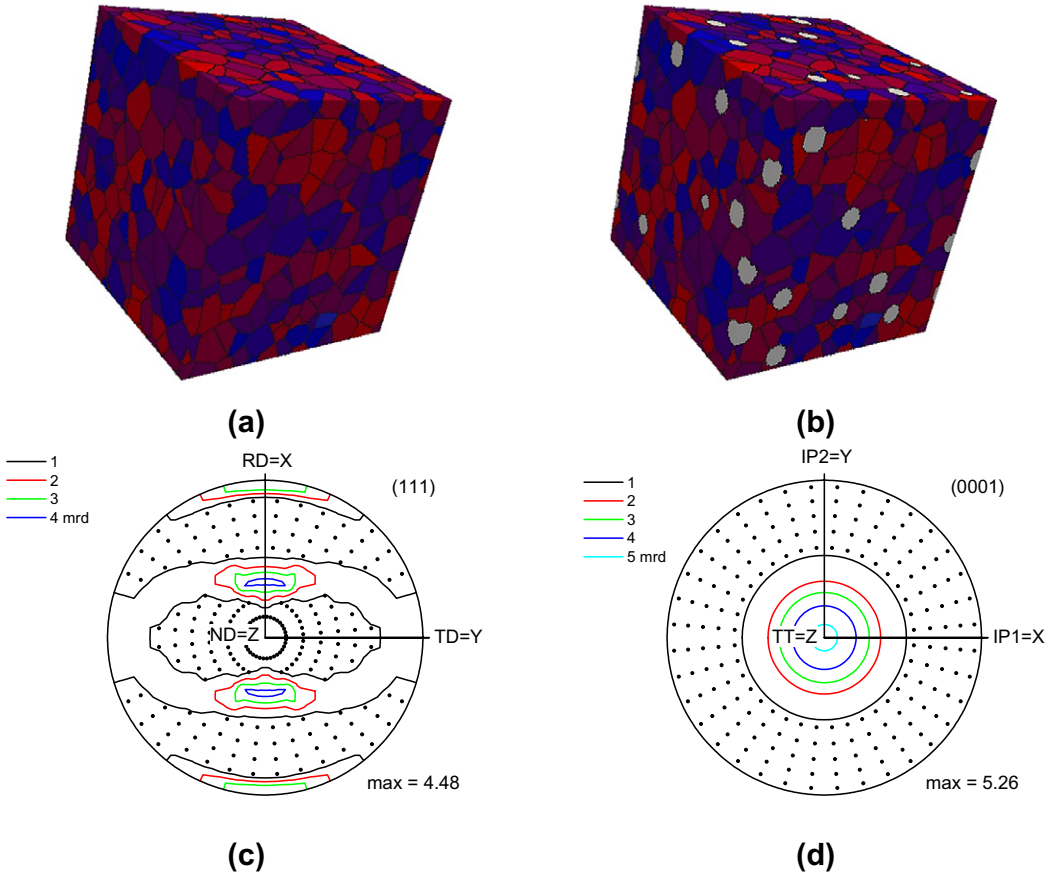

Fig. 1. Unit cells and textures used in FFT simulations. (a) fully-dense polycrystal with 1000 grains, generated by Voronoi tessellation; (b) voided polycrystal with the same 1000 grains and 100 voids (5% porosity) obtained by means of the void seeding procedure explained in Section 3.1. In the cases of unit cells representing isotropic fcc and bcc polycrystals, grain orientations were randomly assigned from a Sobol (1967) sequence of orientations for cubic symmetry. In the cases of unit cells representing textured polycrystals, the sets of 1000 orientations assigned to the grains correspond to: (c) fcc polycrystal with orthotropic texture, (111) pole figure shown; (d) hcp polycrystal with transversely isotropic texture, basal pole figure shown. Intensity lines correspond to multiples of random distribution (mrd). Dots correspond to regions of the pole figures with intensities lower than that of random distribution (1 mrd).

follows a $128 \times 128 \times 128$ grid was used). Each Fourier point was assigned to its nearest nucleus (see Fig. 1a). Additionally, to generate porous polycrystals, all Fourier points at multiple junctions were identified and picked in a random sequence to try to accommodate a cavity centered in that point of a radius r_1 and surrounded by a "security" zone of radius $r_1 + r_2$ where no other cavity was allowed. These radii were adjusted such that the target porosity was reached. Fig. 1b shows the resulting unit cell, representing a porous polycrystal with 1000 grains, 109 voids and 5% porosity, obtained by setting $r_1 = 6$ and $r_2 = 6.35$ (in units of distance between adjacent Fourier points). Three different sets of 1000 orientations were assigned to the single crystal domains. In the case of isotropic (i.e. uniform texture or "untextured") fcc and bcc polycrystals (see Section 4.1), the orientations were chosen from a Sobol (1967) sequence of orientations, in order to generate polycrystals with an effective response as close as possible to isotropy (Brenner et al., 2009). In the case of textured fcc (Section 4.2) and hcp polycrystals (Section 4.3), the orientations were chosen to represent the fcc orthotropic texture shown in Fig. 1c, and the transversely-isotropic hcp texture of Fig. 1d, respectively.

3.2. FFT-based algorithm for voided polycrystals

The discretization of the periodic unit cells described above determines a regular grid in the Cartesian space **{x}** and a corresponding grid of the same size in Fourier space **{k}**. The determination of gauge functions (see below) requires a stress to be imposed to the unit cell. Under this boundary condition, the local strain rate field, a function of the local velocity field, can be split into its average and a fluctuation term (denoted by "∼"):

$$\dot{\varepsilon}_{ij}(\mathbf{v}(\mathbf{x})) = \dot{E}_{ij} + \tilde{\dot{\varepsilon}}_{ij}(\tilde{\mathbf{v}}(\mathbf{x})) \tag{28}$$

The local constitutive relation between the strain rate and the stress for material points (i.e. belonging to grains) is given by the rate-sensitivity equation (Asaro and Needleman, 1985):

$$\dot{\varepsilon}(\mathbf{x}) = \dot{\gamma}_o \sum_{k=1}^{N_k} \mathbf{m}^k(\mathbf{x}) \left(\frac{|\mathbf{m}^k(\mathbf{x}) : \boldsymbol{\sigma}(\mathbf{x})|}{\tau_o^k(\mathbf{x})} \right)^n \mathrm{sgn}(\mathbf{m}^k(\mathbf{x}) : \boldsymbol{\sigma}(\mathbf{x})), \tag{29}$$

where $\tau_o^k(\mathbf{x})$ and $\mathbf{m}^k(\mathbf{x})$ are, respectively, the critical resolved shear stress (CRSS) and the Schmid tensor, associated with each slip or twinning system k of the N_k systems available, $\dot{\gamma}_o$ is a normalization factor, and n is the stress exponent. The strain rate in material points has no dilatational component. As for the Fourier points belonging to voids, the stress vanishes and the strain rate is non-traceless in general and needs to be determined. A fourth-order tensor $\mathbf{L}^o$ is chosen as the stiffness of a linear reference medium, and a polarization field is calculated as:

$$\varphi_{ij}(\mathbf{x}) = \tilde{\sigma}_{ij}(\mathbf{x}) - L^o_{ijkl} \tilde{\dot{\varepsilon}}_{kl}(\mathbf{x}). \tag{30}$$

Therefore, the stress deviation can be written as:

$$\tilde{\sigma}_{ij}(\mathbf{x}) = L^o_{ijkl}\tilde{\tilde{\varepsilon}}_{kl}(\mathbf{x}) + \varphi_{ij}(\mathbf{x}), \tag{31}$$

which, combined with the equilibrium condition and $\tilde{\tilde{\varepsilon}}_{kl}(\mathbf{x}) = sym(\tilde{v}_{k,l}(\mathbf{x}))$ gives:

$$L^o_{ijkl}\tilde{v}_{k,lj}(\mathbf{x}) + \varphi_{ij,j}(\mathbf{x}) = 0. \tag{32}$$

The differential equation for the Green function of the velocity field is then given by:

$$L^o_{ijkl}G_{km,lj}(\mathbf{x}-\mathbf{x}') + \delta_{im}\delta(\mathbf{x}-\mathbf{x}') = 0. \tag{33}$$

After some manipulation (see Lebensohn et al., 2011), the convolution integral that gives the velocity deviation field is:

$$\tilde{v}_k(\mathbf{x}) = \int_{R^3} G_{ki,j}(\mathbf{x}-\mathbf{x}')\varphi_{ij}(\mathbf{x}')d\mathbf{x}', \tag{34}$$

which, written in Fourier space allows us to obtain (Lebensohn et al. 2011):

$$\hat{\tilde{v}}_{i,j}(\mathbf{k}) = \hat{\Gamma}_{ijkl}(\mathbf{k})\hat{\varphi}_{kl}(\mathbf{k}) \tag{35}$$

where the symbol "^" indicates a Fourier transform and $\Gamma_{ijkl} = G_{ik,jl}$. The operators in Eqs. (34) and (35) can be calculated in Fourier space as: $\hat{G}_{ij}(\mathbf{k}) = A^{-1}_{ij}(\mathbf{k})$, where: $A_{ik}(\mathbf{k}) = k_l k_j L^o_{ijkl}$, and $\hat{\Gamma}_{ijkl}(\mathbf{k}) = -k_j k_l \hat{G}_{ik}(\mathbf{k})$.

The iterative procedure of Michel et al. (2000), based on an augmented Lagrangians algorithm, was adapted (Lebensohn et al., 2011) to the case of porous polycrystals, as follows. Supra-indices in parenthesis indicate values corresponding to the current iteration (e.g. "(0)" indicates the initial guess). The algorithm for a full stress tensor $\boldsymbol{\Sigma}$ imposed to the unit cell needs an initial guess for the average strain rate:

$$\dot{E}^{(0)}_{ij} = \dot{E}'^{(0)}_{ij} + \frac{\dot{E}^{(0)}_{kk}}{3}\delta_{ij}, \tag{36}$$

which will be adjusted iteratively. Initial guess values also need to be assigned to the strain rate field in the regular grid:

$$\tilde{\tilde{\dot{\varepsilon}}}'^{(0)}_{ij}(\mathbf{x}) = 0 \Rightarrow \dot{\varepsilon}'^{(0)}_{ij}(\mathbf{x}) = \dot{E}'_{ij} \quad (\mathbf{x} \in \text{material and voids}), \tag{37}$$

$$\tilde{\tilde{\dot{\varepsilon}}}^{(0)}_{kk}(\mathbf{x}) = -\dot{E}_{kk} \Rightarrow \dot{\varepsilon}^{(0)}_{kk}(\mathbf{x}) = 0 \quad (\mathbf{x} \in \text{material}), \tag{38}$$

$$\tilde{\tilde{\dot{\varepsilon}}}^{(0)}_{kk}(\mathbf{x}) = \left(\frac{1}{f} - 1\right)\dot{E}_{kk} \quad (\mathbf{x} \in \text{voids}). \tag{39}$$

With these initial values, the corresponding stress field in the crystalline material points $\boldsymbol{\sigma}^{(0)}(\mathbf{x})$ is obtained inverting the local constitutive relation (Eq. (29)). As for the points belonging to voids, the stress simply vanishes. The initial specification of these fields allows us to calculate the initial guess for the polarization field in direct space (Eq. (30)), which can be, in turn, Fourier-transformed. Furthermore, assuming:

$$\lambda^{(0)}_{ij}(\mathbf{x}) = \sigma^{(0)}_{ij}(\mathbf{x}) \tag{40}$$

as initial guess for an auxiliary stress field associated with the compatibility constraint, the iterative procedure reads as follows. With the polarization field after iteration *(i)* being known, the $(i+1)$-th iteration starts by computing the new guess for the kinematically-admissible strain rate fluctuation field:

$$\hat{\tilde{d}}^{(i+1)}_{ij}(\mathbf{k}) = -\hat{\Gamma}^{sym}_{ijkl}(\mathbf{k})\hat{\varphi}^{(i)}_{kl}(\mathbf{k}), \quad \forall \mathbf{k} \neq \mathbf{0}; \quad \text{and} \quad \hat{\tilde{d}}^{(i+1)}_{ij}(\mathbf{0}) = \mathbf{0}. \tag{41}$$

The corresponding field in real space is thus obtained by application of the inverse FFT, and the new guess for the stress field in the grains is calculated from:

$$\boldsymbol{\sigma}^{(i+1)}(\mathbf{x}) + \mathbf{L}^o : \tilde{\boldsymbol{\varepsilon}}^{(i+1)}(\mathbf{x}) = \boldsymbol{\lambda}^{(i)}(\mathbf{x}) + \mathbf{L}^o : (\dot{\mathbf{E}}^{(i)} + \tilde{\mathbf{d}}^{(i+1)}(\mathbf{x})), \tag{42}$$

which, combined with Eq. (29), gives a 6×6 system of nonlinear algebraic equations to solve for $\boldsymbol{\sigma}^{(i+1)}(\mathbf{x})$. The iteration is completed with the calculation of new guesses for the Lagrange multiplier field:

$$\boldsymbol{\lambda}^{(i+1)}(\mathbf{x}) = \boldsymbol{\lambda}^{(i)}(\mathbf{x}) + \mathbf{L}^o : (\tilde{\tilde{\boldsymbol{\varepsilon}}}^{(i+1)}(\mathbf{x}) - \tilde{\mathbf{d}}^{(i+1)}(\mathbf{x})) \tag{43}$$

and the new guess for the average strain rate (Michel et al., 2001):

$$\dot{\mathbf{E}}^{(i+1)} = \langle \dot{\boldsymbol{\varepsilon}}^{(i)}(\mathbf{x}) \rangle + \mathbf{L}^{o^{-1}} : (\boldsymbol{\Sigma} - \langle \boldsymbol{\sigma}^{(i+1)}(\mathbf{x}) \rangle), \tag{44}$$

where <.> indicates average over the entire Fourier grid. The algorithm then advances until the normalized average differences between the stress fields $\boldsymbol{\sigma}(\mathbf{x})$ and $\boldsymbol{\lambda}(\mathbf{x})$ and strain rate fields $\dot{\boldsymbol{\varepsilon}}(\mathbf{x})$ and $\mathbf{d}(\mathbf{x})$ are smaller than a threshold.

3.3. Gauge functions

The constitutive equation (29) derives from a single-crystal stress potential defined as:

$$u(\mathbf{x}, \boldsymbol{\sigma}) = \sum_{k=1}^{N_k} \frac{\dot{\gamma}_o \tau^k_o(\mathbf{x})}{n+1}\left(\frac{|\mathbf{m}^k(\mathbf{x}) : \boldsymbol{\sigma}(\mathbf{x})|}{\tau^k_o(\mathbf{x})}\right)^{n+1} \tag{45}$$

such that: $\dot{\varepsilon}(\mathbf{x}) = \partial u(\mathbf{x}, \boldsymbol{\sigma})/\partial \boldsymbol{\sigma}$. Moreover, in a porous polycrystal, the stress potential inside a void is $u(\mathbf{x}, \boldsymbol{\sigma}) = 0$ if $\boldsymbol{\sigma} = 0$ and infinity otherwise. The effective viscoplastic behavior of the aggregate is defined as the relation between the average stress $\boldsymbol{\Sigma} = <\boldsymbol{\sigma}(\mathbf{x})>$ and the average strain rate $\dot{\mathbf{E}} = <\dot{\boldsymbol{\varepsilon}}(\mathbf{x})>$ over the aggregate. Formally, it is given by:

$$\dot{\mathbf{E}} = \frac{\partial U}{\partial \boldsymbol{\Sigma}}(\Sigma); \quad U(\Sigma) = \min_{\boldsymbol{\sigma} \in S(\Sigma)} \langle u(\mathbf{x}, \boldsymbol{\sigma}) \rangle, \tag{46}$$

where $U(\Sigma)$ is the effective stress potential for the aggregate and $S(\Sigma)$ denotes the set of statically-admissible stress fields with prescribed average Σ .

The local potentials are in this case homogeneous functions of degree (n + 1) in $\boldsymbol{\sigma}$, and consequently, the corresponding effective potential $U(\Sigma)$ is a homogeneous function of degree (n + 1) in Σ (Ponte Castañeda and Suquet, 1998). Then, a single equipotential surface: $U(\Sigma) =$ constant, fully characterizes U; any other equipotential surface is simply a homothetic surface (Leblond et al., 1994). Results for power-law polycrystals are reported here in the form of equipotential surfaces given by:

$$\left\{\Sigma^* : U(\Sigma^*) = \frac{\sigma_o^{-n}\dot{\gamma}_o}{n+1}\right\}, \tag{47}$$

where σ_o is some reference flow stress (specific choices for σ_o are discussed in Section 4.1). This is the so-called gauge surface of the polycrystal, which characterizes completely the effective response (Leblond et al., 1994). A more convenient equation for the gauge surface can be obtained by writing the effective potential as:

$$U(\Sigma) = \frac{\sigma_o \dot{\gamma}_o}{n+1}\left(\frac{\Lambda(\Sigma)}{\sigma_o}\right)^{n+1} \tag{48}$$

where the so-called gauge factor $\Lambda(\boldsymbol{\Sigma})$ is a homogeneous function of degree 1 in $\boldsymbol{\Sigma}$, and $\boldsymbol{\Sigma}^* = \boldsymbol{\Sigma}/\Lambda(\boldsymbol{\Sigma})$ lies on the gauge surface. Thus, we can obtain points of the gauge surface by computing the effective stress potential for an applied macroscopic stress of arbitrary magnitude, determining the corresponding gauge factor from Eq. (48), and rescaling the applied stress accordingly.

Before ending this section, the implications of comparing gauge surfaces obtained for a unit cell consisting of a rate-sensitive material with distributed porosity (see Fig. 1b) with analytical yield surfaces obtained from limit analysis for a rate-insensitive hollow sphere should be acknowledged. Due to the distinct characteristics of the FFT-based and analytical models, i.e. distributed porosity in

a periodic medium vs. hollow sphere geometry, exact full-field solution vs. upper-bound estimate, and rate-sensitive vs. rate-insensitive plasticity of the matrix, the comparison between the predictions of the models should be regarded as qualitative, rather than strictly quantitative.

Specifically, for a stress exponent n = 10 (see Eq. (29)), adopted throughout this work to guarantee convergence of the FFT-based algorithm, the gauge surface of a porous material with such viscoplastic behavior will differ from the yield surface of an analogous rate-insensitive material, the exact difference depending on porosity and triaxiality. The order of the expected difference can be exemplified by comparing the rate-insensitive Gurson (1977) model and the rate-sensitive Gurson extension of Leblond et al. (1994) (LPS model). For 5% porosity, the difference between the LPS gauge surface and Gurson's yield surface varies from −2% (LPS softer Gurson) to +4% (LPS harder than Gurson), going from purely deviatoric to purely hydrostatic loadings. Also, the consideration of distributed porosity is known to imply stronger void interaction, and therefore a slightly softer effective response, compared with the hollow sphere solution (Lebensohn et al., 2011). Finally, the use of a single unit cell (of relatively large but still limited size, i.e. not necessarily an RVE) may also imply some deviation from the analytical results, although the latter has been mitigated in the cases of isotropic behavior by the use of a Sobol sequence of orientations (see Section 3.1), and by checking that the differences in the predicted axisymmetric behavior of the resulting unit cell, deformed along each axis, was minimal.

4. Results

4.1. Isotropic porous materials

Let us first compare the analytical yield loci for isotropic porous materials with matrix exhibiting "strength-differential", according to Cazacu and Stewart (2009), with corresponding gauge surfaces of fcc and bcc polycrystals with uniform texture and tension–compression asymmetry induced by constituent grains deforming by twinning, obtained with the full-field approach of Lebensohn et al. (2011).

For isotropic porous materials, the analytic yield criterion is given by Eq. (20) and involves only one material parameter, k, that characterizes the tension–compression asymmetry ratio, σ_T/σ_C, of the matrix, such that (Cazacu et al., 2006):

$$k = \frac{1-\alpha(\sigma_T/\sigma_C)}{1+\alpha(\sigma_T/\sigma_C)}, \tag{49}$$

with:

$$\alpha = \sqrt{\frac{2-\left(\frac{\sigma_T}{\sigma_C}\right)^2}{2\left(\frac{\sigma_T}{\sigma_C}\right)^2-1}}. \tag{50}$$

For polycrystals, a first batch of simulations was carried out for an untextured fcc aggregate, considering $\{111\}<11\bar{2}>$ twinning as the only deformation mechanism at the single crystal level. The FFT-based model predicts for this artificial fully-dense fcc isotropic polycrystal a ratio $\sigma_T/\sigma_C = 0.83$, which corresponds to k = −0.3014 (note that only two flow stresses, corresponding to uniaxial tension and compression were necessary for this determination). It is worth noting that considering a more realistic single crystal deformation (e.g. for low stacking-fault energy (SFE) fcc materials) by a combination of slip and twinning, the difference between the uniaxial yield stresses in tension and compression would have been smaller, but of the same sign (Hosford and Allen, 1973). Fig. 2a shows the yield locus predicted by the isotropic form of the CPB06 criterion (Eq. (27)) for k = −0.3014, in comparison with points of the gauge surface (symbols) belonging to the π-plane (i.e. plane normal the hydrostatic axis) predicted with the FFT-based model, obtained by probing the untextured full-dense polycrystal of Fig. 1a with strain rates imposed every 10° on the π-plane. Clearly, this non-trivial agreement implies that the isotropic CPB06 criterion describes very well the plastic behavior of the fully-dense fcc polycrystal with uniform texture.

For an untextured bcc polycrystal deforming by twinning only, the "strength-differential" is just the opposite of the one predicted for the above fcc material. Fig. 2b shows similar comparison between points of the gauge function for an untextured fully-dense bcc polycrystal deforming solely by $\{112\}\langle\bar{1}\bar{1}1\rangle$ twinning, and the yield locus according to the isotropic CPB06 criterion. The FFT-based model predicts a ratio $\sigma_C/\sigma_T = 0.83$ (the reciprocal of the ratio for the fcc polycrystal) which, according to Eqs. (49) and (50), corresponds to k = 0.3014 (minus the fcc value). Again, the tension–compression asymmetry of the fully-dense isotropic bcc polycrystal is very well captured by the CPB06 yield criterion.

Considering now the cases of porous fcc and bcc polycrystals of the type described above, Figs. 3 and 4 show points belonging to the gauge surfaces, corresponding to $f = 0.05$ and stress-triaxialities $X_\sigma = 0, \pm0.5, \pm1.5, \pm2.5, \pm6, \pm20, \pm\infty$, obtained by means of the FFT-based approach, together with the analytical yield loci according to Cazacu and Stewart (2009), in the plane $(\sigma_m/\sigma_T, \sigma_e/\sigma_T)$, for axisymmetric loadings corresponding to either $J_3 \geqslant 0$ or $J_3 \leqslant 0$ (for axisymmetric loading conditions, only the sensitivity to the sign of the third invariant can be assessed). The tensile stress of the fully-dense polycrystal, σ_T, is used as normalization factor, such that, for the calculation of the gauge surface points (Eq. (48)) we imposed $\sigma_o = \sigma_T$. Note that, in all cases, the surfaces are smooth at the purely hydrostatic points (i.e. no corners) (see also, Revil-Baudard and Cazacu, 2012).

The main observation from these figures is that the strong effect of the third invariant of the stress deviator on the dilatational response, predicted by Cazacu and Stewart's (2009) criterion is indeed confirmed by the full-field results. For the porous fcc polycrystal, whose matrix is softer in tension than in compression ($\sigma_T/\sigma_C = 0.83$), the FFT predictions corresponding to $J_3 < 0$ are above those for $J_3 > 0$. The maximum split, corresponding to purely deviatoric loading, is given by: $\frac{\sigma_e|_{X_\sigma=0 J_3>0}}{\sigma_e|_{X_\sigma=0 J_3>0}} = \frac{0.9186}{1.077} = 0.8529$. Meanwhile, for the porous bcc polycrystal, whose matrix is softer in compression than in tension ($\sigma_C/\sigma_T = 0.83$), the opposite occurs i.e. the FFT predictions corresponding to $J_3 > 0$ are above those for $J_3 < 0$, with the maximum split being: $\frac{\sigma_e|_{X_\sigma=0 J_3<0}}{\sigma_e|_{X_\sigma=0 J_3>0}} = \frac{0.7698}{0.9018} = 0.8536$. Thus, within the precision of the numerical solutions, the maximum splits for the fcc and bcc polycrystals are identical, as they should be.

On the other hand, according to Cazacu and Stewart's (2009) criterion, for a material with matrix having $\sigma_T < \sigma_C$ ($\sigma_C < \sigma_T$, respectively) as in the case for the porous fcc (respectively, bcc) polycrystal, the yield points corresponding to $J_3 < 0$ should be higher (respectively, lower) than that for $J_3 > 0$. Furthermore, for $J_3 < 0$, the intersection of the analytical yield locus with the deviatoric axis is (see Eq. (25a)):

$$(\sigma_e/\sigma_T)|_{\sigma_m=0 J_3<0} = (1-f)\left(\frac{\sigma_C}{\sigma_T}\right), \tag{51}$$

while, for $J_3 > 0$, the intersection is at:

$$(\sigma_e/\sigma_T)|_{\sigma_m=0 J_3>0} = 1-f. \tag{52}$$

Thus, the maximum split between the yield loci for the fcc porous polycrystal is: $\frac{(\sigma_e/\sigma_T)|_{\sigma_m=0 J_3>0}}{(\sigma_e/\sigma_T)|_{\sigma_m=0 J_3<0}} = \frac{\sigma_T}{\sigma_C} = 0.83$, while for the bcc porous polycrystal, the maximum split between the yield loci is:

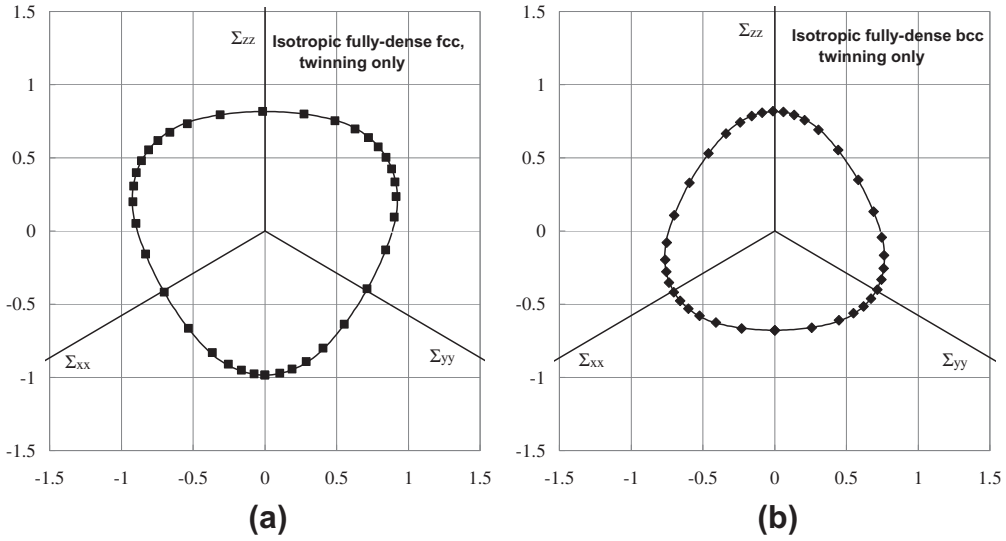

Fig. 2. Comparison between π-plane projections of gauge surfaces predicted with the FFT-based approach for fully-dense (a) fcc and (b) bcc polycrystals with uniform texture deforming solely by twinning (symbols), with yield surfaces (line) according to the isotropic form of CPB06 yield criterion (Eq. (27)).

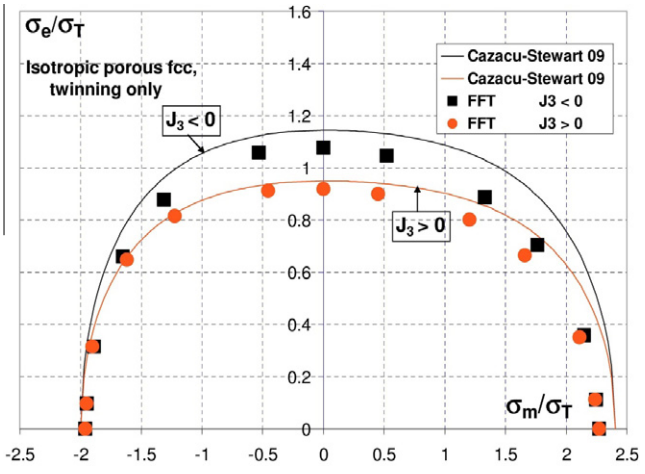

Fig. 3. Comparison between gauge surfaces from FFT full-field simulations (symbols) of a fcc polycrystalline porous material ($f = 0.05$) with uniform texture deforming solely by twinning, with Cazacu and Stewart's (2009) yield surfaces (lines) for a matrix displaying tension–compression asymmetry $\sigma_T/\sigma_C = 0.83$ ($k = -0.3014$), for axisymmetric loadings with $J_3 \geqslant 0$ and $J_3 \leqslant 0$.

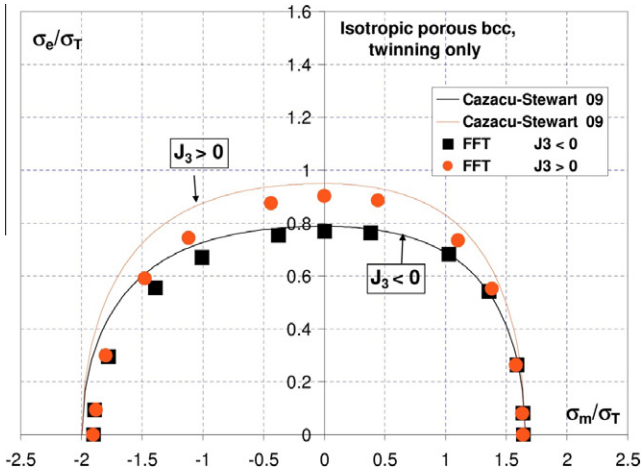

Fig. 4. Comparison between gauge surfaces from FFT full-field simulations (symbols) of a bcc polycrystalline porous material ($f = 0.05$) with uniform texture deforming solely by twinning, with Cazacu and Stewart's (2009) yield surfaces (lines) for a matrix displaying tension–compression asymmetry $\sigma_C/\sigma_T = 0.83$ ($k = 0.3014$), for axisymmetric loadings with $J_3 \geqslant 0$ and $J_3 \leqslant 0$.

$\frac{(\sigma_e/\sigma_T)|_{\sigma_m=0 J_3<0}}{(\sigma_e/\sigma_T)|_{\sigma_m=0 J_3>0}} = \frac{\sigma_C}{\sigma_T} = 0.83$. Thus, the maximum splits for the Cazacu–Stewart's (2009) materials representing the fcc and bcc polycrystals, are the same, and very close, but not identical, to the FFT predictions.

While the numerical predictions of the maximum split (i.e. for purely deviatoric loading) between surfaces for the porous polycrystals are close to the analytical value, the purely deviatoric responses predicted by the FFT-based method for the both types of polycrystals are softer than those given by Cazacu and Stewart's (2009) criterion. This softer behavior predicted by the full-field approach is to be expected since, in the derivation of the analytic plastic potential, homogenization was carried out using Rice and Tracey's (1969) velocity field. While for hydrostatic loading this velocity field is the only field compatible with uniform strain-rate boundary conditions, and, consequently, the purely hydrostatic estimates coincide with the exact solution for the hollow sphere (see also Cazacu and Stewart, 2009), this field is less accurate (stiffer) for purely deviatoric loading (see also Nahshon and Hutchinson, 2008).

Note also that the full-field predictions for the porous polycrystals show a clear effect of the sign of applied hydrostatic loading on the material's response. For the voided fcc polycrystal, with matrix having $\sigma_T < \sigma_C$, the FFT prediction corresponding to tensile hydrostatic loading ($X_\sigma = \infty$) is larger than the one corresponding to compressive hydrostatic loading ($X_\sigma = -\infty$), the ratio being: $\frac{|\sigma_m|_{X_\sigma=-\infty}|}{\sigma_m|_{X_\sigma=\infty}} = \frac{1.958}{2.272} = 0.8618$. For the voided bcc polycrystal, with matrix having $\sigma_T > \sigma_C$, the FFT prediction corresponding to compressive hydrostatic loading is larger than the one corresponding to tensile hydrostatic loading, i.e. $\frac{\sigma_m|_{X_\sigma=\infty}}{|\sigma_m|_{X_\sigma=-\infty}|} = \frac{1.639}{1.903} = 0.8613$, i.e. identical, within the precision of the numerical solutions, as they should be. On the other hand, the intersections of the analytical yield loci with the hydrostatic axis are (see Eqs. (23) and (24)): $\sigma_m/\sigma_T|_{X_\sigma=\infty} = p_Y^T/\sigma_T = -\frac{2}{3}(\frac{\sigma_C}{\sigma_T})\ln(f)$ and $\sigma_m/\sigma_T|_{X_\sigma=-\infty} = p_Y^C/\sigma_T = \frac{2}{3}\ln(f)$, respectively. Therefore, for the voided fcc polycrystal, $\frac{\sigma_m|_{X_\sigma=\infty}}{|\sigma_m|_{X_\sigma=-\infty}|} = \frac{\sigma_T}{\sigma_C} = 0.83$ (and reciprocal, in the bcc case), which is very close, but not identical, to the full-field predictions.

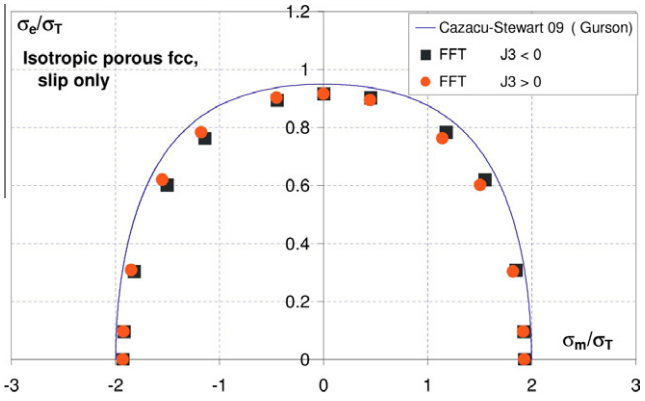

Fig. 5. Gauge surfaces (symbols) predicted with the FFT-based approach for axisymmetric loadings with $J_3 \geqslant 0$ and $J_3 \leqslant 0$, respectively, for a porous ($f = 0.05$) fcc polycrystal with uniform texture, deforming solely by slip, in comparison with Cazacu and Stewart's (2009) yield function (lines) for $\sigma_T/\sigma_C = 1$ ($k = 0$), which in this case is unique and coincides with Gurson's (1977) model.

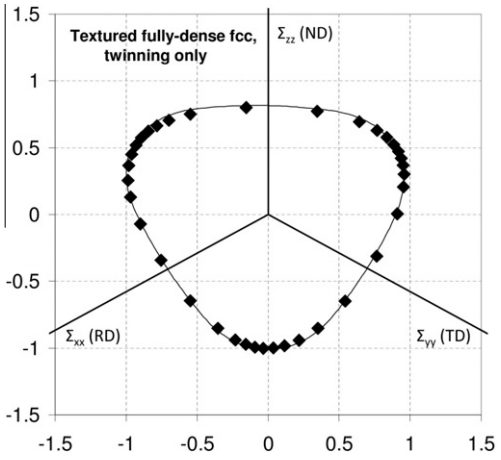

Fig. 6. Comparison between the π-plane projection of the gauge surface predicted with the FFT-based approach for a fully-dense fcc polycrystal with orthotropic texture deforming solely by twinning (symbols), with yield surfaces (line) according to the orthotropic CPB06 yield criterion (Eq. (10)).

Comparison between the full-field results and Cazacu and Stewart's (2009) model are also presented for an isotropic porous material with a matrix that does not display tension–compression asymmetry (Fig. 5). As already mentioned, in the case of a matrix with no "strength-differential" effects, Cazacu and Stewart (2009) reduces to Gurson (1977). Specifically, adopting {111}<110> slip obeying Schmid law as plastic deformation mechanism at single crystal level for the untextured fcc polycrystal, the fcc polycrystalline matrix has no tension–compression asymmetry, i.e. $\sigma_T = \sigma_C$, $k = 0$, and the isotropic form of Cazacu et al. (2006) reduces to von Mises criterion (see Eq. (27)). Under these conditions, the yield surface for $J_3 \geqslant 0$ coincides with that for $J_3 \leqslant 0$ (see Eqs. (25)). The FFT-based calculations for the voided polycrystal with no tension–compression asymmetry confirm that: (a) the purely deviatoric point is insensitive to the sign of J_3, and (b) the yielding of the porous aggregate under purely hydrostatic loading does not depend on the sense of loading. Interestingly, for stress-triaxialities different from 0 and $\pm\infty$, the full-field predictions do differ (slightly) depending on the sign of the third invariant. The same trend was observed by means of standard FE unit cell calculations by Cazacu and Stewart (2009). Moreover, the numerical results show that a point belonging to one of the gauge surfaces (e.g. $J_3 \geqslant 0$) corresponding to a given stress-triaxiality X_σ is symmetric, with respect to the deviatoric axis, to the point on the other gauge surface (e.g. $J_3 \leqslant 0$) corresponding to $-X_\sigma$. To our knowledge, this very specific dependence on the third invariant of the dilatational plastic behavior of porous materials predicted with full-field approaches has not been realized before, and may deserve more attention in the future.

4.2. Textured porous fcc polycrystals

In this section, Stewart and Cazacu's (2011) criterion is applied to represent a porous fcc polycrystal with orthotropic texture (see Fig. 1c). The material parameters involved in the CPB06 criterion are the coefficients L_{ij} and the "strength-differential" parameter k that describe the anisotropic and asymmetric plastic response of the fully-dense matrix material, respectively. The numerical values of these parameters are determined using the uniaxial tensile and compressive flow stresses along the axes of orthotropy, calculated using FFT-based simulations for the fully-dense polycrystal. As in the previous isotropic case, the deformation mode at single crystal level was assumed to be $\{111\}<11\bar{2}>$ twinning. The full-field simulations predict for the solid material: $\sigma_x^C/\sigma_x^T = 1.273$; $\sigma_y^T/\sigma_x^T = 0.985$; $\sigma_y^C/\sigma_x^T = 1.311$; $\sigma_z^T/\sigma_x^T = 0.962$; and $\sigma_z^C/\sigma_x^T = 1.226$. The numerical values of the CPB06 coefficients are: $L_{12} = 0.0315$, $L_{13} = -0.0076$, $L_{22} = 1.0373$, $L_{23} = 0.0224$, $L_{33} = 0.9958$, with the coefficient L_{11} set to 1 (due to the homogeneity in stresses of the criterion), and $k = -0.43$ (see Cazacu et al. (2006) for further details on the identification procedure).

Fig. 6 shows points of the gauge surfaces belonging to the π-plane obtained with the FFT-based model by probing the textured (see Fig. 1c) full-dense polycrystal (Fig. 1a) with strain rates imposed every 10° on the π-plane, together with the yield locus according to the orthotropic CPB06 criterion corresponding to the values of L_{ij} and the "strength-differential" parameter k previously identified. Note the very good agreement between the orthotropic CPB06 criterion and the polycrystalline gauge surface for the fully-dense textured polycrystal.

To illustrate the combined effects of anisotropy and tension–compression asymmetry of the matrix on the yielding of the textured porous ($f = 0.05$) fcc polycrystal, Fig. 7 shows points belonging to the gauge surfaces calculated with the FFT-based approach, and the Stewart and Cazacu's (2011) yield loci in the plane (σ_m/σ_T, $-\sigma_e/\sigma_T$) for J_3 positive and J_3 negative, corresponding to axisymmetric loadings. Let us start with the discussion of the predictions corresponding to purely hydrostatic loading, i.e. $\boldsymbol{\sigma} = \sigma_m(\mathbf{x}\otimes\mathbf{x} + \mathbf{z}\otimes\mathbf{z} + \mathbf{y}\otimes\mathbf{y})$. These points are the same in all three figures, as they should be. The FFT results show the effect of the sense of applied hydrostatic loading on the response of the porous material. For this voided orthotropic fcc polycrystal, the mean stress corresponding to tensile hydrostatic loading is larger than the absolute value of the yield pressure corresponding to compressive hydrostatic loading (see Fig. 7a–c), the ratio being equal to 1.159. According to the analytic criterion, the ratio between the tensile and compressive hydrostatic pressure is $\sqrt{\frac{3k^2-2k+3}{3k^2+2k+3}}$ (see Eqs. (12) and (13)), which for $k = -0.43$ corresponds to 1.280.

Moreover, according to Stewart and Cazacu's (2011) criterion, for axisymmetric loadings the sensitivity of the dilatational response of the porous material to the third-invariant of the stress deviator can be correlated to the matrix tension–compression asymmetry ratio in the direction corresponding to the major principal stress. These trends are confirmed by the FFT results. For example, in the case of axisymmetric loading along the x-axis (Fig. 7a), the FFT yield locus for $J_3 < 0$ is above that corresponding to $J_3 > 0$. This trend is correctly described by Stewart and Cazacu's (2011) criterion, according to which, in the present case of a matrix having $\sigma_x^C/\sigma_x^T > 1$, the yield surface corresponding to $J_3 < 0$ is above that for $J_3 > 0$. For example, for purely deviatoric loading,

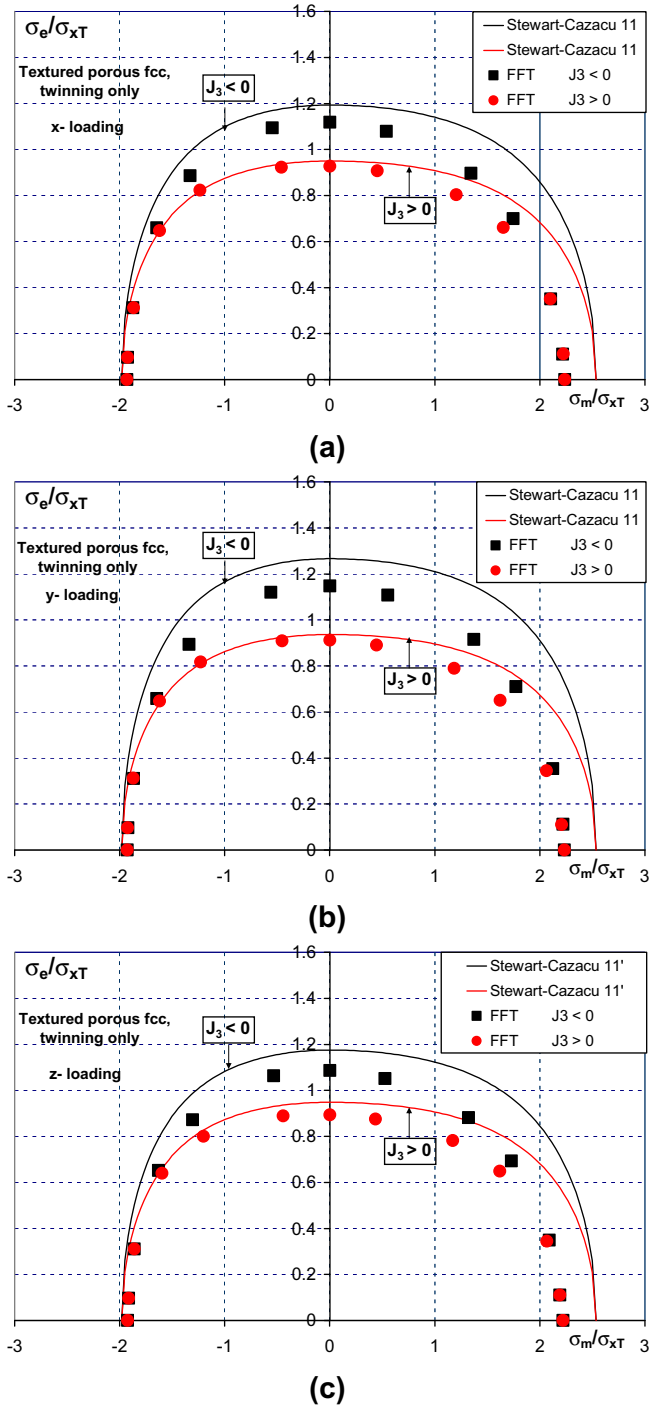

Fig. 7. Comparison between gauge surfaces (symbols) from full-field simulations of a porous ($f = 0.05$) textured (orthotropic) fcc polycrystal and yield surfaces (lines) obtained with Stewart and Cazacu's (2011) anisotropic criterion (Eq. (1)). Cases for $J_3 \geqslant 0$ and $J_3 \leqslant 0$. Axisymmetric loading along: (a) x-axis (RD); (b) y-axis (TD), and (c) z-axis (ND).

the FFT-based model predicts $\frac{\sigma_e|_{X_\sigma=0 J_3>0}}{\sigma_e|_{X_\sigma=0 J_3<0}} = \frac{0.9407}{1.134} = 0.8395$, while according to the analytical model, yielding occurs when $\sigma_e = (1-f)\sigma_x^C$ for $J_3 \leqslant 0$ (see Eq. (14a)), and $\sigma_e = (1-f)\sigma_x^T$ for $J_3 > 0$ (see Eq. (14b)), resulting in a ratio $\frac{\sigma_e|_{X_\sigma=0 J_3>0}}{\sigma_e|_{X_\sigma=0 J_3<0}} = \frac{\sigma_x^T}{\sigma_x^C} = \frac{1}{1.273} = 0.7855$.

Similar trends are observed for axisymmetric loading along the y-axis and z-axis, respectively. This is due to the fact that the orthotropic matrix is characterized by $\sigma_y^C/\sigma_y^T > 1$ and $\sigma_z^C/\sigma_z^T > 1$. Note that the FFT prediction of the split between the J_3-positive and J_3-negative curves is most pronounced for y-loading, consistent with the analytical values, given by: $\frac{\sigma_y^T}{\sigma_y^C} = 0.7401 < \frac{\sigma_x^T}{\sigma_x^C} = 0.7855 \cong \frac{\sigma_z^T}{\sigma_z^C} = 0.7847$.

4.3. Textured porous hcp polycrystals

In this section, Stewart and Cazacu's (2011) criterion is applied to represent a porous hcp polycrystal with transversely-isotropic texture (see Fig. 1d). The numerical values of L_{ij} and k are determined using the uniaxial tensile and compressive strengths along the axis of rotational symmetry, i.e. the "through-thickness" (TT) direction (z-axis) in Fig. 1d, and the uniaxial tensile and compressive strengths along any direction belonging to the plane of isotropy of the material i.e. an "in-plane" (IP) direction (e.g. x-axis) in Fig. 1d, calculated using FFT-based simulations for the fully-dense polycrystal. The deformation modes adopted at single crystal level are the soft {1010}<1210>prismatic (pr) slip, the hard {1122}<1123>pyramidal <c+a>(pyr) slip, and the {1102}<1011> soft tensile twinning (ttw), for a c/a ratio of 1.594. The relative CRSSs of these modes are (see Eq. (29)): $\tau_o^{ttw}/\tau_o^{pr} = 1$, $\tau_o^{pyr}/\tau_o^{pr} = 3.5$. For these relative CRSSs values, a textured polycrystal with <c>-axes predominantly oriented in the TT direction (see Fig. 1d) exhibits a strong tension–compression asymmetry (tension softer than compression) along the TT axis. Unlike the fcc cases, an hcp polycrystal with this kind of texture and active slip and twinning systems is representative of the behavior of real metallic systems, like Zr at room temperature (e.g. see Tomé et al., 2001). The full-field simulations predict for the solid material: $\sigma_x^C/\sigma_x^T = 0.9112$; $\sigma_z^T/\sigma_x^T = 1.007$; and $\sigma_z^C/\sigma_x^T = 1.363$. Setting $L_{11} = 1$, the numerical values of the CPB06 parameters are: $L_{12} = -0.198$, $L_{13} = L_{23} = 0.424$, $L_{22} = L_{11} = 1$, $L_{33} = 1.675$, and $k = -0.167$.

Fig. 8 shows points of the gauge surfaces belonging to the π-plane obtained with the FFT-based model, by probing the full-dense polycrystal of Fig. 1a with texture given by Fig. 1d, with strain rates imposed every 10° on the π-plane, and the yield locus according to the anisotropic CPB06 criterion (Eq. (10)) with the values of L_{ij} and the "strength-differential" parameter k previously identified. Once again, a good agreement between the transversely-isotropic CPB06 criterion and the polycrystalline gauge surface of the fully-dense hcp polycrystal was obtained.

To illustrate the combined effects of anisotropy and tension–compression asymmetry of the matrix on yielding of the textured porous ($f = 0.05$) hcp polycrystal, Fig. 9 shows the points belonging to the gauge surfaces calculated with the FFT-based approach, and Stewart and Cazacu's (2011) yield loci in the plane $(\sigma_m/\sigma_T, \sigma_e/\sigma_T)$ for J_3 positive and J_3 negative, corresponding to axisymmetric loadings with the axial stress along the TT axis and the IP axis, respectively. In this case, the effect of the sense of applied hydrostatic loading on the response of the porous material predicted by the FFT-based is very mild, compared with the analytical prediction, as it can be appreciated in both Fig. 9a and b. According to the analytic criterion, the absolute value of the yield pressure corresponding to compressive hydrostatic loading is larger than that corresponding to tensile hydrostatic loading. For the identified $k = -0.167$, this ratio is 1.115. According to FFT-based model, the absolute value of the yield pressure corresponding to compressive hydrostatic loading is slightly larger than the mean stress corresponding to tensile hydrostatic loading, with a ratio of 1.019.

Despite the above underestimation of the asymmetry of the purely hydrostatic response, the strong effect of the third stress invariant predicted by the Stewart–Cazacu's (2011) criterion is well reproduced by the FFT-based calculations. In the case of loading along an in-plane direction (Fig. 9a), both the analytical and numerical predictions corresponding to stress states for which $J_3 > 0$ are

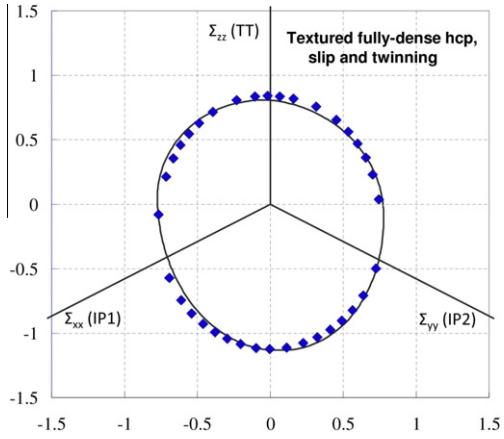

Fig. 8. Comparison between the π-plane projection of the gauge surface predicted with the FFT-based approach for a fully-dense hcp polycrystal with transversely-isotropic texture deforming by slip and twinning (symbols), with the corresponding yield surfaces (line) according to the transversely-isotropic form of CPB06 yield criterion (Eq. (10)).

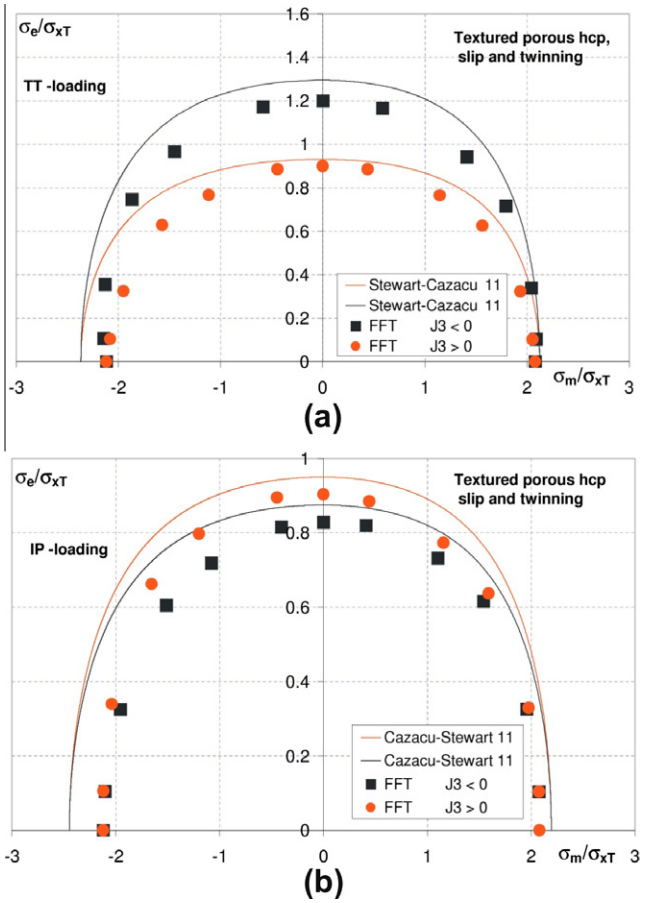

Fig. 9. Comparison between gauge surfaces (symbols) from full-field simulations of a porous ($f = 0.05$) textured (transversely-isotropic) hcp polycrystal and yield surfaces (lines) obtained with Stewart and Cazacu's (2011) anisotropic criterion (Eq. (1)). Cases for $J_3 \geqslant 0$ and $J_3 \leqslant 0$. Axisymmetric loading along: (a) in-plane (IP) directions, (b) through-thickness (TT), respectively.

above that corresponding to $J_3 < 0$. This trend is consistent with the matrix material having $\sigma_x^C/\sigma_x^T < 1$. For purely deviatoric loading, according to the analytical model (either Eqs. (14a) and (14b) or Eqs. (15a) and (15b)), the ratio is $\frac{\sigma_e|_{X_\sigma=0,J_3<0}}{\sigma_e|_{X_\sigma=0,J_3>0}} = \frac{\sigma_x^C}{\sigma_x^T} = 0.9112$, while the FFT-based model predicts $\frac{\sigma_e|_{X_\sigma=0,J_3<0}}{\sigma_e|_{X_\sigma=0,J_3>0}} = \frac{0.8286}{0.9031} = 0.9175$. Reversed trend is observed for axisymmetric loading along the TT direction, for which $\sigma_z^C/\sigma_z^T > 1$. The analytical value (see Eqs. (16a) and (16b)) is: $\frac{\sigma_e|_{X_\sigma=0,J_3<0}}{\sigma_e|_{X_\sigma=0,J_3>0}} = \frac{\sigma_z^C}{\sigma_z^T} = 1.353$, and the numerical prediction is: $\frac{\sigma_e|_{X_\sigma=0,J_3<0}}{\sigma_e|_{X_\sigma=0,J_3>0}} = \frac{1.200}{0.901} = 1.332$.

5. Conclusions and perspectives

In this paper, the combined effects of intrinsic single-crystal deformation mechanisms and texture on the overall plastic response of voided polycrystals were assessed for the first time. In doing this, the dilatational viscoplastic FFT-based approach of Lebensohn et al. (2011) was used to generate gauge surfaces of these materials, which were in turn compared with the analytical yield surfaces for voided isotropic and anisotropic materials according to Stewart and Cazacu's (2011) criterion.

The FFT-based predictions showed a clear effect of the sense of applied hydrostatic loading on the response of porous polycrystalline materials for which the intrinsic single-crystal plastic deformation mechanisms are sensitive to the sign of the resolved shear stress. The gauge surfaces for voided isotropic fcc and bcc polycrystals deforming only by twinning are no longer symmetric with respect to the deviatoric axis. A strong influence of the third invariant of the stress deviator on the dilatational response was clearly demonstrated. For verification purposes, FFT-based simulations for a porous isotropic fcc material with no "strength-differential" (i.e. single crystal deforming by slip only) were also carried out. The resulting gauge surface was symmetric with respect to the deviatoric axis, the influence of the third invariant was small (but not negligible), and except for the latter, the overall agreement with Gurson's (1977) yield surface was good.

In the case of a textured fcc polycrystal deforming only by twinning, it was shown that the strong sensitivity to the sign of the third invariant is due to the directionality of the tension–compression asymmetry of this material. In particular, the most pronounced split between the cases for J_3 positive and J_3 negative was obtained in the direction of the highest contrast between the matrix's yield in tension and compression. For the textured hcp polycrystal deforming by slip and twinning, the tension–compression asymmetry in the plastic flow for pure hydrostatic loadings is less pronounced, but still, the same trends of the dilatational response are revealed.

All these unusual features of the dilatational response of voided materials in which the matrix is incompressible, but yet displays tension–compression asymmetry, namely: the lack of symmetry of the yield surfaces with respect to both the hydrostatic and deviatoric axes, are also predicted by the analytical criterion of Stewart and Cazacu (2011). Although the agreement obtained between the numerical FFT predictions and the analytical results is not necessarily quantitative (due to different assumptions involved in both approximations to the problem of dilatational plasticity), the good qualitative agreement serves as a cross-validation of both approaches. The noticeable effects related to microstructural tension–compression asymmetry and texture-induced anisotropy revealed here deserve to be further investigated experimentally.

Note also that the analytic criterion can be efficiently implemented as material subroutine in FE codes for engineering applications involving polycrystalline materials with such complex dilatational plastic behavior, requiring the identification of a number of materials parameters. This identification can be done using experimental data, simulations, or a combination of both (e.g. Plunkett et al., 2006, 2007). If microstructure evolution affects

the overall asymmetric/anisotropic response of the aggregate, these materials parameters may need to be updated, as well.

While in the examples shown here the source of the tension–compression asymmetry of the plastic flow of polycrystalline aggregates was ascribed to constituent single crystals deforming by twinning, this "strength-differential" at polycrystal level may arise from other single-crystal plasticity mechanisms, like the already mentioned non-Schmid effects in bcc metals (Groger et al., 2008), or, e.g. when different components of the applied stress affect the single crystal plastic deformation by climb, for aggregates deforming in the creep regime (Lebensohn et al., 2010). For modeling porosity evolution in these materials and regimes, Stewart–Cazacu's (2011) extension of the Gurson model may prove to be very valuable to capture microstructural effects on void growth, in an efficient closed-form fashion.

Acknowledgments

R.A.L. acknowledges support from LANL's Joint DoD/DOE Munitions Technology Program and ASC Physics & Engineering Models, Materials Project. O.C. acknowledges partial financial support from NSF (Grant CMMI-1000303) and AFOSR Grant FA9550-10-1-0429.

Appendix A. Components of the anisotropic tensor B

The components (in Voigt notation) of tensor **B** used in Eq. (8) are:

$$B_{12}=\frac{1}{3}\cdot\frac{2(C_{32}-C_{12})+(C_{31}-C_{11})}{(C_{21}-C_{11})(C_{32}-C_{12})-(C_{22}-C_{12})(C_{31}-C_{11})}, \tag{A1}$$

$$B_{13}=\frac{1}{3}\cdot\frac{(C_{11}-C_{21})+2(C_{22}-C_{12})}{(C_{11}-C_{21})(C_{32}-C_{22})-(-C_{22}+C_{12})(C_{31}-C_{21})}, \tag{A2}$$

$$B_{11}=-(B_{12}+B_{13}), \tag{A3}$$

$$B_{21}=B_{12}, \tag{A4}$$

$$B_{23}=\frac{1}{3}\cdot\frac{2(C_{11}-C_{21})+(C_{12}-C_{22})}{(C_{11}-C_{21})(C_{32}-C_{22})-(-C_{22}+C_{12})(C_{31}-C_{21})}, \tag{A5}$$

$$B_{22}=-(B_{21}+B_{23}), \tag{A6}$$

$$B_{31}=B_{13}, \tag{A7}$$

$$B_{32}=B_{23}, \tag{A8}$$

$$B_{33}=-(B_{31}+B_{23}), \tag{A9}$$

$$B_{44}=\frac{1}{C_{44}}, \tag{A10}$$

$$B_{55}=\frac{1}{C_{55}}, \tag{A11}$$

$$B_{66}=\frac{1}{C_{66}}. \tag{A12}$$

Appendix B. Expressions of the Stewart and Cazacu's (2011) anisotropic criterion for axisymmetric loadings

To illustrate the dependence of the Stewart and Cazacu (2011) criterion (Eq. (1)) on all invariants of $\boldsymbol{\sigma}'$ and on the mixed invariants associated with the orthotropy of the matrix, in what follows we deduce the expressions of this criterion for axisymmetric loadings. To simplify the equations, we introduce the following notation:

$$\Phi_1=\frac{1}{3}(2\,L_{11}-\,L_{12}-\,L_{13}),\quad \Phi_2=\frac{1}{3}(2L_{12}-L_{22}-L_{23}),$$
$$\Phi_3=\frac{1}{3}(2L_{13}-\,L_{23}-\,L_{33}) \tag{B1}$$

$$\Psi_1=\frac{1}{3}(-L_{11}+2L_{12}-L_{13}),\quad \Psi_2=\frac{1}{3}(-L_{12}+2L_{22}-L_{23}),$$
$$\Psi_3=\frac{1}{3}(-L_{13}+2L_{23}-L_{33}) \tag{B2}$$

$$\Lambda_1=\frac{1}{3}(-L_{11}-\,L_{12}+2\,L_{13}),\quad \Lambda_2=\frac{1}{3}(-L_{12}-\,L_{22}+2L_{23}),$$
$$\Lambda_3=\frac{1}{3}(-L_{13}-\,L_{23}+2\,L_{33}) \tag{B3}$$

In all cases, σ_1 will denote the axial stress while σ_3 will denote the lateral stress (i.e. the value of the two principal stresses that are equal). Thus, irrespective of the orientation of the loading reference system with respect to the reference system associated to the orthotropy of the matrix, the von Mises equivalent stress is $\sigma_e=|\sigma_1-\sigma_3|$, the mean stress is $\sigma_m=(\sigma_1+2\sigma_3)/3$, and the deviatoric third invariant is $J_3=\frac{2}{27}(\sigma_1-\sigma_3)^3$.

Case. 1: axisymmetric loading along the x-axis of orthotropy

The axial stress is along the *x*-axis, while the lateral stresses along the y-axis and *z*-axis are equal, i.e.

$$\boldsymbol{\sigma}=\sigma_1(\mathbf{x}\otimes\mathbf{x})+\sigma_3(\mathbf{y}\otimes\mathbf{y}+\mathbf{z}\otimes\mathbf{z}) \tag{B4}$$

For such loading, $\sigma'_1=\frac{2}{3}(\sigma_1-\sigma_3)\sigma'_2=\sigma'_3=-\frac{1}{3}(\sigma_1-\sigma_3)$ and the principal values of the transformed stress $\hat{\boldsymbol{\sigma}}=\boldsymbol{L}:\boldsymbol{\sigma}'$ are:

$$\hat{\sigma}_1=\Phi_1(\sigma_1-\sigma_3),\quad \hat{\sigma}_2=\Phi_2(\sigma_1-\sigma_3),\quad \text{and}$$
$$\hat{\sigma}_3=\Phi_3(\sigma_1-\sigma_3) \tag{B5}$$

Case. 1(a): $J_3\leqslant 0$ (i.e. $\sigma_1\leqslant\sigma_3$)

Substituting the principal values of the transformed stress tensor (Eq. (B5)) in the expression of the CPB06's effective stress (Eq. (10)):

$$\tilde{\sigma}_e=\hat{m}\sqrt{\sum_{i=1}^{3}(|\hat{\sigma}_i|-k\hat{\sigma}_i)^2}=\hat{m}\;|\sigma_1-\sigma_3|$$
$$\sqrt{(|\Phi_1|+k\Phi_1)^2+(|\Phi_2|+k\Phi_2)^2+(|\Phi_3|+k\Phi_3)^2}$$
$$=|\sigma_1-\sigma_3|\sqrt{\frac{(|\Phi_1|+k\Phi_1)^2+(|\Phi_2|+k\Phi_2)^2+(|\Phi_3|+k\Phi_3)^2}{(|\Phi_1|-k\Phi_1)^2+(|\Phi_2|-k\Phi_2)^2+(|\Phi_3|-k\Phi_3)^2}}. \tag{B6}$$

According to the CPB06 criterion, the ratio between the matrix's uniaxial tensile yield stress and its compressive yield stress in the x-direction is (see Cazacu et al., 2006):

$$\frac{\sigma_x^C}{\sigma_x^T}=\sqrt{\frac{(|\Phi_1|-k\Phi_1)^2+(|\Phi_2|-k\Phi_2)^2+(|\Phi_3|-k\Phi_3)^2}{(|\Phi_1|+k\Phi_1)^2+(|\Phi_2|+k\Phi_2)^2+(|\Phi_3|+k\Phi_3)^2}}. \tag{B7}$$

So, with (B6) and (B7) we obtain:

$$\tilde{\sigma}_e=|\sigma_1-\sigma_3|\cdot\left(\frac{\sigma_x^T}{\sigma_x^C}\right)=\sigma_e\cdot\left(\frac{\sigma_x^T}{\sigma_x^C}\right). \tag{B8}$$

Thus, for axisymmetric loading along the *x*-axis corresponding to $J_3\leqslant 0$, criterion (1) becomes Eq. (14a).

Case. 1(b): $J_3 \geqslant 0$ *(i.e.* $\sigma_1 \geqslant \sigma_3$*)*

In this case, the CPB06's effective stress is:

$$\begin{aligned}\tilde{\sigma}_e &= \hat{m}\sqrt{\sum_{i=1}^{3}(|\hat{\sigma}_i| - k\hat{\sigma}_i)^2} \\ &= \hat{m}|\sigma_1-\sigma_3|\sqrt{(|\Phi_1| - k\Phi_1)^2 + (|\Phi_2| - k\Phi_2)^2 + (|\Phi_3| - k\Phi_3)^2}\end{aligned} \tag{B9}$$

Using Eq. (4) that expresses $\hat{m}$ in terms of the anisotropy coefficients and parameter k, we obtain:

$$\tilde{\sigma}_e = |\sigma_1 - \sigma_3| = \sigma_e \tag{B10}$$

Thus, for axisymmetric loading along x-axis corresponding to $J_3 \geqslant 0$, the Stewart and Cazacu's (2011) criterion is given by Eq. (14b).

Case. 2: axisymmetric loading along the y-axis of orthotropy

The axial stress is along the y-axis, while the lateral stresses along the x-axis and z-axis are equal, i.e.

$$\boldsymbol{\sigma} = \sigma_1(\mathbf{y}\otimes\mathbf{y}) + \sigma_3(\mathbf{x}\otimes\mathbf{x} + \mathbf{z}\otimes\mathbf{z}) \tag{B11}$$

For such loading, $\sigma'_1 = \sigma'_3 = -\frac{1}{3}(\sigma_1 - \sigma_3)$; $\sigma'_2 = \frac{2}{3}(\sigma_1 - \sigma_3)$, and the principal values of the transformed stress are:

$$\begin{aligned}&\hat{\sigma}_1 = \Psi_1(\sigma_1 - \sigma_3), \hat{\sigma}_2 = \Psi_2(\sigma_1 - \sigma_3), \quad \text{and} \\ &\hat{\sigma}_3 = \Psi_3(\sigma_1 - \sigma_3)\end{aligned} \tag{B12}$$

Case. 2(a): $J_3 \leqslant 0$ *(i.e.* $\sigma_1 \leqslant \sigma_3$*)*

Substituting the principal values of the transformed stress tensor (Eq. (B12)) in the expression of CPB06's effective stress:

$$\begin{aligned}\tilde{\sigma}_e &= \hat{m}\sqrt{\sum_{i=1}^{3}(|\hat{\sigma}_i| - k\hat{\sigma}_i)^2} \\ &= \hat{m}|\sigma_1-\sigma_3|\sqrt{(|\Psi_1| + k\Psi_1)^2 + (|\Psi_2| + k\Psi_2)^2 + (|\Psi_3| + k\Psi_3)^2} \\ &= |\sigma_1-\sigma_3|\sqrt{\frac{(|\Psi_1| + k\Psi_1)^2 + (|\Psi_2| + k\Psi_2)^2 + (|\Psi_3| + k\Psi_3)^2}{(|\Phi_1| - k\Phi_1)^2 + (|\Phi_2| - k\Phi_2)^2 + (|\Phi_3| - k\Phi_3)^2}}\end{aligned} \tag{B13}$$

According to the CPB06 criterion, the ratio between the matrix's uniaxial tensile yield stresses in the x-direction and its uniaxial compressive yield stress in the y-direction is:

$$\frac{\sigma_x^T}{\sigma_y^C} = \sqrt{\frac{(|\Psi_1| + k\Psi_1)^2 + (|\Psi_2| + k\Psi_2)^2 + (|\Psi_3| + k\Psi_3)^2}{(|\Phi_1| - k\Phi_1)^2 + (|\Phi_2| - k\Phi_2)^2 + (|\Phi_3| - k\Phi_3)^2}}. \tag{B14}$$

So, we obtain:

$$\tilde{\sigma}_e = |\sigma_1 - \sigma_3| \cdot \left(\frac{\sigma_x^T}{\sigma_y^C}\right) = \sigma_e \cdot \left(\frac{\sigma_x^T}{\sigma_y^C}\right). \tag{B15}$$

Thus, for axisymmetric loading along y-axis corresponding to $J_3 \leqslant 0$, the Stewart and Cazacu's (2011) criterion is given by Eq. (15a).

Case. 2(b): $J_3 \geqslant 0$ *(i.e.* $\sigma_1 \geqslant \sigma_3$*)*

In this case, CPB06's effective stress becomes:

$$\begin{aligned}\tilde{\sigma}_e &= \hat{m}\sqrt{\sum_{i=1}^{3}(|\hat{\sigma}_i| - k\hat{\sigma}_i)^2} \\ &= \hat{m}|\sigma_1-\sigma_3|\sqrt{(|\Psi_1| - k\Psi_1)^2 + (|\Psi_2| - k\Psi_2)^2 + (|\Psi_3| - k\Psi_3)^2} \\ &= |\sigma_1-\sigma_3|\sqrt{\frac{(|\Psi_1| - k\Psi_1)^2 + (|\Psi_2| - k\Psi_2)^2 + (|\Psi_3| - k\Psi_3)^2}{(|\Phi_1| - k\Phi_1)^2 + (|\Phi_2| - k\Phi_2)^2 + (|\Phi_3| - k\Phi_3)^2}}.\end{aligned} \tag{B16}$$

Since according to the CPB06 criterion, the ratio between the matrix's uniaxial tensile yield stress in the x-direction and its uniaxial tensile yield stresses in the y-direction is:

$$\frac{\sigma_x^T}{\sigma_y^T} = \sqrt{\frac{(|\Psi_1| - k\Psi_1)^2 + (|\Psi_2| - k\Psi_2)^2 + (|\Psi_3| - k\Psi_3)^2}{(|\Phi_1| - k\Phi_1)^2 + (|\Phi_2| - k\Phi_2)^2 + (|\Phi_3| - k\Phi_3)^2}} \tag{B17}$$

we obtain:

$$\tilde{\sigma}_e = |\sigma_1 - \sigma_3| \cdot \left(\frac{\sigma_x^T}{\sigma_y^T}\right) = \sigma_e \cdot \left(\frac{\sigma_x^T}{\sigma_y^T}\right) \tag{B18}$$

Thus, for axisymmetric loading along the y-axis corresponding to $J_3 \geqslant 0$, Stewart and Cazacu's (2011) criterion is given by Eq. (15b).

Case. 3: axisymmetric loading along the z-axis of orthotropy

The axial stress is along the z-axis, and the lateral stresses along the x-axis and y-axis are equal, i.e.

$$\boldsymbol{\sigma} = \sigma_1(\mathbf{z}\otimes\mathbf{z}) + \sigma_3(\mathbf{x}\otimes\mathbf{x} + \mathbf{y}\otimes\mathbf{y}) \tag{B19}$$

For such loading, $\sigma'_1 = \sigma'_2 = -\frac{1}{3}(\sigma_1 - \sigma_3)$; $\sigma'_3 = \frac{2}{3}(\sigma_1 - \sigma_3)$, and the principal values of the transformed stress are:

$$\hat{\sigma}_1 = \Lambda_1(\sigma_1 - \sigma_3), \quad \hat{\sigma}_2 = \Lambda_2(\sigma_1 - \sigma_3), \quad \text{and} \quad \hat{\sigma}_3 = \Lambda_3(\sigma_1 - \sigma_3). \tag{B20}$$

Case. 3(a): $J_3 \leqslant 0$ *(i.e.* $\sigma_1 \leqslant \sigma_3$*)*

Substituting the principal values of the transformed stress tensor (Eq. (B20)) in the expression of CPB06's effective stress:

$$\begin{aligned}\tilde{\sigma}_e &= \hat{m}\sqrt{\sum_{i=1}^{3}(|\hat{\sigma}_i| - k\hat{\sigma}_i)^2} \\ &= \hat{m}|\sigma_1-\sigma_3|\sqrt{(|\Lambda_1| + k\Lambda_1)^2 + (|\Lambda_2| + k\Lambda_2)^2 + (|\Lambda_3| + k\Lambda_3)^2} \\ &= |\sigma_1-\sigma_3|\sqrt{\frac{(|\Lambda_1| + k\Lambda_1)^2 + (|\Lambda_2| + k\Lambda_2)^2 + (|\Lambda_3| + k\Lambda_3)^2}{(|\Phi_1| - k\Phi_1)^2 + (|\Phi_2| - k\Phi_2)^2 + (|\Phi_3| - k\Phi_3)^2}}.\end{aligned} \tag{B21}$$

According to the CPB06 criterion, the ratio between the matrix's uniaxial tensile yield stresses in the x-direction and its uniaxial compressive yield stress in the z-direction is:

$$\frac{\sigma_x^T}{\sigma_z^C} = \sqrt{\frac{(|\Lambda_1| + k\Lambda_1)^2 + (|\Lambda_2| + k\Lambda_2)^2 + (|\Lambda_3| + k\Lambda_3)^2}{(|\Phi_1| - k\Phi_1)^2 + (|\Phi_2| - k\Phi_2)^2 + (|\Phi_3| - k\Phi_3)^2}} \tag{B22}$$

and we obtain:

$$\tilde{\sigma}_e = |\sigma_1 - \sigma_3| \cdot \left(\frac{\sigma_x^T}{\sigma_z^C}\right) = \sigma_e \cdot \left(\frac{\sigma_x^T}{\sigma_z^C}\right). \tag{B23}$$

Thus, for axisymmetric loading along the z-axis corresponding to $J_3 \leqslant 0$, the criterion (1) is given by Eq. (16a).

Case. 3(b): $J_3 \geqslant 0$ (i.e. $\sigma_1 \geqslant \sigma_3$)

CPB06's effective stress becomes

$$\begin{aligned}\tilde{\sigma}_e &= \hat{m}\sqrt{\sum_{i=1}^{3}(|\hat{\sigma}_i| - k\hat{\sigma}_i)^2} \\ &= \hat{m}|\sigma_1 - \sigma_3|\sqrt{(|\Lambda_1| - k\Lambda_1)^2 + (|\Lambda_2| - k\Lambda_2)^2 + (|\Lambda_3| - k\Lambda_3)^2} \\ &= |\sigma_1 - \sigma_3|\sqrt{\frac{(|\Lambda_1| - k\Lambda_1)^2 + (|\Lambda_2| - k\Lambda_2)^2 + (|\Lambda_3| - k\Lambda_3)^2}{(|\Phi_1| - k\Phi_1)^2 + (|\Phi_2| - k\Phi_2)^2 + (|\Phi_3| - k\Phi_3)^2}}.\end{aligned} \tag{B24}$$

According to the CPB06 criterion, the ratio between the matrix's uniaxial tensile yield stress in the *x*-direction and its uniaxial tensile yield stresses in the *z*-direction is:

$$\frac{\sigma_x^T}{\sigma_z^T} = \sqrt{\frac{(|\Lambda_1| - k\Lambda_1)^2 + (|\Lambda_2| - k\Lambda_2)^2 + (|\Lambda_3| - k\Lambda_3)^2}{(|\Phi_1| - k\Phi_1)^2 + (|\Phi_2| - k\Phi_2)^2 + (|\Phi_3| - k\Phi_3)^2}} \tag{B25}$$

and:

$$\tilde{\sigma}_e = |\sigma_1 - \sigma_3| \cdot \left(\frac{\sigma_x^T}{\sigma_z^T}\right) = \sigma_e \cdot \left(\frac{\sigma_x^T}{\sigma_z^T}\right). \tag{B26}$$

Thus, for axisymmetric loading along the *z*-axis corresponding to $J_3 \geqslant 0$, Stewart and Cazacu's (2011) criterion is given by Eq. (16b).

References

Asaro, R.J., Needleman, A., 1985. Texture development and strain hardening in rate dependent polycrystals. Acta Metall. 33, 923–953.

Benzerga, A.A., Besson, J., 2001. Plastic potentials for anisotropic porous solids. Eur. J. Mech. A/Solids 20, 397–434.

Boehler, J.P.,1987. Application of tensors functions in solids mechanics. CISM courses and lectures. In: International Center for Mechanical Sciences, vol. 292, Springer-Verlag, Wien, New York.

Brenner, R., Lebensohn, R.A., Castelnau, O., 2009. Elastic anisotropy and yield surface estimates of polycrystals. Int. J. Solids Struct. 46, 3018–3026.

Cazacu, O., Stewart, J., 2009. Analytic plastic potential for porous aggregates with matrix exhibiting tension–compression asymmetry. J. Mech. Phys. Solids 57, 325–341.

Cazacu, O., Plunkett, B., Barlat, F., 2006. Orthotropic yield criterion for hexagonal closed packed metals. Int. J. Plasticity 22, 1171–1194.

Cuitino, A.M., Ortiz, M., 1996. Ductile fracture by vacancy condensation in fcc single crystals. Acta Metall. 44 (2), 427–436.

DeBotton, G., Ponte Castañeda, P., 1995. Variational estimates for the creep behaviour of polycrystals. Proc. Roy. Soc. A 448, 121–142.

Escobedo, J.P., Cerreta, E.K., Dennis-Koller, D., Patterson, B.M., Bronkhorst, C., Hansen, B., Tonks, D., Lebensohn, R.A., 2011. Effects of grain size and boundary structure on the dynamic tensile response of copper. J. Appl. Phys. 110, 033513.

Garajeu, M., Suquet, P., 1997. Effective properties of porous ideally plastic or viscoplastic materials containing rigid particles. J. Mech. Phys. Solids 45, 873–902.

Gologanu, M., Leblond, J.-B., Perrin, G., Devaux, J., 1997. Recent extension of Gurson model for porous plastic ductile media. In: Suquet, P. (Ed.), Continuum Micromechanics. Springer-Verlag, New York, pp. 61–130.

Gray III, G.T., Bourne, N.K., Zocher, M.A., Maudlin, P.J., Millett, J.C.F., 2000. Influence of crystallographic anisotropy on the Hopkinson fracture spallation of zirconium. In: Furnish, M.D., Chhabildas, L.C., Hixson, R.S. (Eds.), Shock Compression of Condensed Matter 1999. AIP Press, Woodbury, NY, pp. 509–512.

Groger, R., Racherla, V., Bassani, J.L., Vitek, V., 2008. Multiscale modeling of plastic deformation of molybdenum and tungsten: II. Yield criterion for single crystals based on atomistic studies of glide of 1/2<111> screw dislocations. Acta Mater. 56, 5412–5425.

Gurson, A.L., 1977. Continuum theory of ductile rupture by void nucleation and growth: part I: yield criteria and flow rules for porous ductile media. J. Eng. Mater. Technol. Trans. ASME Ser. H 99, 2–15.

Hill, R., 1967. The essential structure of constitutive laws for metal composites and polycrystals. J. Mech. Phys. Solids 15, 79–95.

Hosford, W.F., Allen, T.J., 1973. Twinning and directional slip as a cause for a strength differential effect. Met. Trans. 4, 1424–1425.

Kysar, J.W., Gan, Y.X., 2007. Cylindrical void in a rigid-ideally plastic single crystal. III: hexagonal closed-packed crystal. Int. J. Plasticity 23, 592–619.

Lebensohn, R.A., 2001. N-site modeling of a 3D viscoplastic polycrystal using fast Fourier transform. Acta Mater. 49, 2723–2737.

Lebensohn, R.A., Castelnau, O., Brenner, R., Gilormini, P., 2005. Study of the antiplane deformation of linear 2-D polycrystals with different microstructures. Int. J. Solids Struct. 42, 5441–5459.

Lebensohn, R.A., Brenner, R., Castelnau, O., Rollett, A.D., 2008. Orientation image-based micromechanical modelling of subgrain texture evolution in polycrystalline copper. Acta Mater. 56, 3914–3926.

Lebensohn, R.A., Montagnat, M., Mansuy, P., Duval, P., Meysonnier, J., Philip, A., 2009. Modeling viscoplastic behavior and heterogenous intracrystalline deformation of columnar ice polycrystals. Acta Mater. 57, 1405–1415.

Lebensohn, R.A., Hartley, C.S., Tomé, C.N., Castelnau, O., 2010. Modelling the mechanical response of polycrystals deforming by climb and glide. Phil. Mag. 90, 567–583.

Lebensohn, R.A., Idiart, M.I., Ponte Castaneda, P., Vincent, P.-G., 2011. Dilatational viscoplasticity of polycrystalline solids with intergranular cavities. Phil. Mag. 91, 3038–3067.

Leblond, J.B., Perrin, G., Suquet, P., 1994. Exact results and approximate models for porous viscoplastic solids. Int. J. Plasticity 10, 213–225.

Liu, Y., Ponte Castañeda, P., 2004. Second-order theory for the effective behavior and field fluctuations in viscoplastic polycrystals. J. Mech. Phys. Solids 52, 467–495.

Livescu, V., Bingert, J.F., Mason, T.A., submitted for publication. Deformation twinning in explosively-driven tantalum. Mater. Sci. Eng. A.

Lubarda, V.A., Schneider, M.S., Kalantar, D.H., Remington, B.A., Meyers, M.A., 2004. Void growth by dislocation emission. Acta Mater. 52, 1397–1408.

Mahajan, S., 1981. Accomodation at deformation twins in bcc metals. Met. Trans. A 12, 379–386.

Mandel, J., 1972. Plasticité classique et viscoplasticité. CISM Courses and Lectures. In: International Center for Mechanical Sciences, vol. 97, Springer-Verlag, Wien, New York.

Marya, M., Hector, L.G., Verma, R., Tong, W., 2006. Microstructural effects of AZ31 magnesium alloy on its tensile deformation and failure behaviors. Mater. Sci. Eng. A 418, 341–356.

McClintock, F.A., 1968. A criterion for ductile fracture by the growth of holes. J. Appl. Mech. Trans. ASME 35, 363–371.

Michel, J.C., Moulinec, H., Suquet, P., 2000. A computational method based on augmented Lagrangians and fast Fourier transforms for composites with high contrast. Comput. Model. Eng. Sci. 1, 79–88.

Michel, J.C., Moulinec, H., Suquet, P., 2001. A computational scheme for linear and non-linear composites with arbitrary phase contrast. Int. J. Numer. Methods Eng. 52, 139–160.

Millett, J.C.F., Whiteman, G., Bourne, N.K., Gray III, G.T., 2008. The role of anisotropy in the response of the titanium alloy Ti-6Al-4V to shock loading. J. Appl. Phys. 104, 073531.

Monchiet, V., Cazacu, O., Charkaluk, E., Kondo, D., 2008. Macroscopic yield criteria for plastic anisotropic materials containing spheroidal voids. Int. J. Plasticity 24, 1158–1189.

Moulinec, H., Suquet, P., 1998. A numerical method for computing the overall response of nonlinear composites with complex microstructure. Comput. Methods Appl. Mech. Eng. 157, 69–94.

Nahshon, K., Hutchinson, J.W., 2008. Modification of the Gurson model for shear failure. Eur. J. Mech. A/Solids 27, 1–17.

Nixon, M.E., Cazacu, O., Lebensohn, R.A., 2010a. Anisotropic response of high-purity alpha-titanium: experimental characterization and constitutive modeling. Int. J. Plasticity 26, 516–532.

Nixon, M.E., Lebensohn, R.A., Cazacu, O., Liu, C., 2010b. Experimental and finite-element analysis of the anisotropic response of high-purity alpha-titanium in bending. Acta Mater. 58, 5759–5767.

Ponte Castañeda, P., 1991. The effective mechanical properties of nonlinear isotropic composites. J. Mech. Phys. Solids 39, 45–71.

Ponte Castañeda, P., 2002. Second-order homogenization estimates for nonlinear composites incorporating field fluctuations: I – theory. J. Mech. Phys. Solids 50, 737–757.

Ponte Castañeda, P., Suquet, P., 1998. Nonlinear composites. Adv. Appl. Mech. 34, 171–302.

Plunkett, B., Lebensohn, R.A., Cazacu, O., Barlat, F., 2006. Evolving yield function of hexagonal materials taking into account texture development and anisotropic hardening. Acta Mater. 54, 4159–4169.

Plunkett, B., Cazacu, O., Lebensohn, R.A., Barlat, F., 2007. Elastic–viscoplastic anisotropic modelling of textured metals and validation using the Taylor cylinder impact test. Int. J. Plasticity 23, 1001–1021.

Proust, G., Tomé, C.N., Kaschner, G.C., 2007. Modeling texture, twinning, and hardening evolution during deformation of hexagonal materials. Acta Mater. 55, 2137–2148.

Revil-Baudard, B., Cazacu, O., in press. The effect of the matrix tension-compression asymmetry on damage evolution in porous plastic solids. Eur. J. Mech. A/Solids, doi: http://dx.doi.org/10.1016/j.euromechsol.2012.05.001.

Rice, J.R., Tracey, D.M., 1969. On the ductile enlargement of voids in triaxial stress fields. J. Mech. Phys. Solids 17, 201–217.

Sobol, I.M., 1967. On the distribution of points in a cube and the approximate evaluation of integrals. USSR Comput. Math. Math. Phys. 7, 86–112.

Stewart, J.B., Cazacu, O., 2011. Analytical yield criterion for an anisotropic material containing spherical voids and exhibiting tension–compression asymmetry. Int. J. Solids. Struct. 48, 357–373.

Tirry, W., Nixon, M., Cazacu, O., Coghe, F., Rabet, L., 2011. The importance of secondary and ternary twinning in compressed Ti. Scripta Mater. 64, 840–843.

Tomé, C.N., Maudlin, P.J., Lebensohn, R.A., Kaschner, G.C., 2001. Mechanical response of zirconium: I. Derivation of a polycrystal constitutive law and finite element analysis. Acta Mater. 49, 3085–3096.

Tvergaard, V., 1981. Infuence of voids on shear band instabilities under plane strain conditions. Int. J. Fracture 17, 389–407.

Tvergaard, V., Needleman, A., 1984. Analysis of the cup-cone fracture in a round tensile bar. Acta Metall. 32 (1), 157–169.

Vitek, V., Mrovec, M., Bassani, J.L., 2004. Influence of non-glide stresses on plastic flow: from atomistic to continuum modeling. Mater. Sci. Eng. A 365, 31–37.